

A Significant Population of Candidate New Members of the ρ Ophiuchi Cluster

Mary Barsony^{1,2}

SETI Institute, 189 Bernardo Ave, Suite 100, Mt. View, CA 94043, mbarsony@seti.org

and

Karl E. Haisch Jr.¹

*Utah Valley University, Physics Dept., 800 W. University Pkwy., Orem, Utah 84058-5999,
Karl.Haisch@uvu.edu*

and

Kenneth A. Marsh

*Infrared Processing and Analysis Center, California Institute of Technology 100-22,
Pasadena, California 91125, kam@ipac.caltech.edu*

and

Chris McCarthy

*San Francisco State University, Dept. of Physics & Astronomy, 1600 Holloway Ave., San
Francisco, California 94132, exoplanet@gmail.com*

ABSTRACT

We present a general method for identifying the pre-main-sequence population of any star-forming region, unbiased with respect to the presence or absence of disks, in contrast to samples selected primarily via their mid-infrared emission from *Spitzer* surveys. We have applied this technique to a new, deep, wide-field,

¹Visiting Astronomer at the Anglo-Australian Telescope, Siding Spring, Australia.

²San Francisco State University, Dept. of Physics & Astronomy, 1600 Holloway Ave., San Francisco, California 94132

near-infrared imaging survey of the ρ Ophiuchi cloud core to search for candidate low mass members. In conjunction with published *Spitzer* IRAC photometry, and least squares fits of model spectra (COND, DUSTY, NextGen, and blackbody) to the observed spectral energy distributions, we have identified 948 candidate cloud members within our 90% completeness limits of $J = 20.0$, $H = 20.0$, and $K_S = 18.50$. This population represents a factor of ~ 3 increase in the number of known young stellar objects in the ρ Ophiuchi cloud. A large fraction of the candidate cluster members ($81\% \pm 3\%$) exhibit infrared excess emission consistent with the presence of disks, thus strengthening the possibility of their being *bona fide* cloud members. Spectroscopic follow-up will confirm the nature of individual objects, better constrain their parameters, and allow an initial mass function to be derived.

Subject headings: ISM: individual objects (ρ Ophiuchi) — stars: pre-main sequence — infrared: stars

1. Introduction

Sub-stellar objects, including brown dwarfs, sub-brown dwarfs, and free-floating objects of planetary mass, are all at their most luminous (by orders of magnitude) upon formation. Therefore, the nearest and youngest star-forming regions (SFRs) present the best opportunity to determine the shape of the initial mass function (IMF) at the lowest masses. Theories of star-formation that attempt to predict IMFs (Kroupa 2011; Hennebelle & Chabrier 2011; McKee & Ostriker 2007), require observational constraints, especially at the low mass end. Specifically, one pressing open question is: What is the lowest mass object that can form via the usual star-formation process?

The advent of large-format near-infrared (NIR) array detectors has opened the door to surveying large angular extents of nearby SFRs with sensitivity sufficient to uncover planetary mass objects. The potential now exists to determine the IMF shapes of the nearest and youngest SFRs through the substellar regime down to $\sim 1\text{--}2\text{ }M_{Jup}$.

Recent work on some nearby SFRs has determined IMFs in a statistical sense only, by deriving luminosity functions (LFs), deduced from imaging data obtained in just a single NIR waveband. For example, IMFs were derived from observed K-band luminosity functions (KLFs) for the Orion Nebula Cluster (ONC— Muench et al. 2002) and IC348 (Muench et al. 2003) or from the observed J-band luminosity function (JLF) for IC348 (Preibisch et al. 2003). This method for IMF determination relies on: *i*) an assumed form

of the mass function, *ii*) an assumed age distribution, and *iii*) pre-main-sequence model tracks which give the single filter brightness for a given mass. Additional complications that arise for this (and other) method(s) of IMF determination include: distinguishing cluster members from non-members, accounting for the extinction to each object, and correcting for excess emission due to circumstellar material/disks to the observed KLF's (this latter effect is minimized for JLFs).

A summary of published IMFs that make use of NIR photometric data for six nearby SFRs is presented in Table 1. Distances, ages, telescope/instrument combinations used, completeness limits reached, and references are listed. The potential for deriving an IMF in ρ Oph is shown by listing the parameters of our survey in the last entry of Table 1.

Alternative approaches for IMF determinations of SFRs, applicable to low extinction regions, include converting the observed JLF to an LF with the aid of model pre-main-sequence tracks by applying bolometric corrections (B.C.'s) derived from field stars. Pre-main-sequence tracks, for a presumed cluster age, are then used to convert the luminosity function to a mass function (e.g., Lodieu et al. 2009) for σ Ori. This approach is aided by complementary spectroscopy, since the B.C.'s are a function of spectral type (e.g., Caballero et al. 2007). Optical multi-object spectroscopy has been used for IMF determinations in relatively low-extinction regions of SFRs to derive cluster membership, extinction, and spectral types for individual candidate young stellar objects (YSOs). Broadband photometry is then used, in conjunction with bolometric corrections, to derive individual YSO luminosities. Each YSO is plotted on an H-R diagram, and comparison with a set of pre-main-sequence tracks is used to derive a mass and age for each cluster member (e.g., Luhman 2004) for Taurus; (Luhman 2007) for Cha I.

Finally, fitting of multi-wavelength spectral energy distributions (SEDs) has been used to derive de-reddened effective temperatures (T_{eff}) for cloud members. Pre-main-sequence tracks, for an assumed cluster age, are then used to derive mass values for a given T_{eff} (e.g., Marsh et al. 2010a) for ρ Oph. This approach, however, is problematic for treating YSOs with circumstellar disks and/or envelopes.

Related to the determination of the shape of the IMF at the lowest masses is the search for a low mass cut-off of the IMF. This search has been the focus of many recent investigations. We list those making use of deep, NIR imaging in Table 2. In the IC348 cluster, one new candidate planetary mass object (PMO) has been proposed but awaits spectroscopic confirmation (Burgess et al. 2009). The most recent deep, large-area, NIR study of the ONC, covered a $30' \times 40'$ region to $J \simeq 19.5$ mag, $H \simeq 18.0$ mag, and $K_s \simeq 18.5$ mag (3σ), a sensitivity sufficient to detect 1 MYr old PMO's to $A_V \simeq 10$ mag of extinction (Robberto et al. 2010). These authors found 1298 sources in the reddened brown dwarf

region and 142 in the reddened PMO region of the H vs. $J - H$ color-magnitude diagram. The source distribution in the corresponding regions of the K_s vs. $H - K_s$ color-magnitude diagram yielded 2134 sources in the reddened brown dwarf region and 421 sources in the reddened PMO region. In NGC1333, no PMO's have been found, but 19 spectroscopically confirmed brown dwarfs have, from a sample of 36 objects with $i' - z'$ colors expected for young, very low mass objects (Scholz et al. 2009). This, despite the sensitivity of the survey to mass limits of $0.008 M_\odot$ for $A_V \leq 10$ mag and $0.004 M_\odot$ for $A_V \leq 5$ mag, led the authors to the conjecture that the low-mass cut-off corresponding to $T_{eff} < 2500$ K has been found for this cluster. In the ChaI SFR, a deep optical imaging survey, with follow-up deep near-infrared photometry, sensitive to mass limits of $0.003 M_\odot - 0.005 M_\odot$ for $A_v \leq 5$, with follow-up low-resolution optical spectroscopy (Mužić et al. 2011), found no new confirmed substellar objects, beyond those found in Luhman (2007). The more recent study placed upper limits on the number of missing planetary mass members (down to $\sim 0.008 M_\odot$) of $\leq 3\%$ (≤ 7) of the currently known YSO population in Chamaeleon I. Due to its large angular extent, searches for PMO's in the Taurus SFR have been targeted towards known members, be they young stellar objects (YSOs) or young brown dwarfs. Two notable PMO candidates discovered in this way, necessarily members of multiple systems, are TMR1-c (Terebey et al. 1998; Riaz & Martín 2011) and 2MASS J04414489+2301513 (Todorov et al. 2010). Large area surveys of Taurus using 2MASS and *Spitzer* data have been used to search for new members, including brown dwarfs (Luhman et al. 2006, 2009a,b; Rebull et al. 2010), bringing the total list of known Taurus members to 318 (Luhman et al. 2010), of which 43 are spectroscopically confirmed as substellar (Monin et al. 2010). In the σ Ori cluster, a careful re-analysis of archival data, supplemented by newer large-area, sensitive imaging, led to the discovery of three new planetary mass candidates down to $\sim 4 M_{Jup}$, bringing to 17 the total number of candidate PMO's in this region (Bihain et al. 2009). In the recent deep NIR imaging study of Lupus III, no planetary mass objects (corresponding to late T spectral types), but 17 sub-stellar candidates (with $1700K \leq T_{eff} \leq 3000K$) have been identified (Comerón 2011).

The subject of this study, the ρ Oph SFR, is an especially attractive target, due to its relatively compact area, proximity ($d=120 \pm 5$ pc—Loinard et al. (2008), richness of its embedded young stellar population (Wilking et al. 2008; Barsony et al. 2005), and youth ~ 1 MYr (Luhman & Rieke 1999; Prato et al. 2003; Wilking et al. 2005). As such, it has been the target of several, deep, large area NIR surveys whose stated aim is finding its lowest mass members. In their sensitive NIR survey of ~ 1 deg² of the main ρ Ophiuchi cloud core, Alves de Oliveira et al. (2010) report the detection of $\sim 5.7 \times 10^4$ objects, which they winnowed down using various color-magnitude diagrams guided by the 1 MYr DUSTY isochrone of Chabrier et al. (2000). Their final list of 110 candidate substellar members includes 80

which are newly identified. Another recent survey searching for the lowest mass member in ρ Oph covered a $31.5' \times 26'$ area in the iJK_s filters. This investigation resulted in the discovery of one new, spectroscopically confirmed, brown dwarf (Geers et al. 2011). Furthermore, these same authors identified 27 brown dwarf candidates (11 of which have previous spectroscopic confirmation) using *Spitzer* photometry. Analysis of the 2MASS calibration strip, running along a $9'$ wide swath through the ρ Oph core, resulted in the identification of 11 possible planetary mass objects ($T \leq 1800\text{K}$) of ~ 115 cluster-member candidates (Marsh et al. 2010a). Follow-up spectroscopy of seven of these resulted in the discovery of a single planetary mass object (Marsh et al. 2010b).

An alternate approach that has been used to search for the lowest mass member of the ρ Oph core is to target the spectroscopic signature of methane (CH_4) absorption, found in low-temperature ($T_{\text{eff}} \leq 1500\text{ K}$) atmospheres. Images are acquired through specially designed adjacent narrow-band methane-off ($\sim 1.6\mu\text{m}$) and methane-on ($\sim 1.7\mu\text{m}$) filters covering the H -band. Methane absorbing objects, that would have masses of $\sim 1\text{--}2 M_{\text{Jup}}$ at the age and distance of the ρ Oph core, would appear uniquely and characteristically bright in methane-off minus methane-on differential images. This technique has been used to survey a 920 arcmin^2 region of the ρ Oph core to identify 22 planetary mass candidates (Haisch, Barsony, & Tinney 2010).

Spectroscopic follow-up of these candidates is currently being carried out by our team. As a part of our ongoing H –band methane-filter imaging program of nearby SFRs to discover their lowest mass members, we are also acquiring complementary deep J and K_s data. In this paper, we report the discovery of 948 candidate low-mass members from combined, deep, JHK_s imaging of the central 920 arcmin^2 area of the ρ Ophiuchi cloud core, supplemented by *Spitzer* data.

The new observations and data reduction methods are described in §2. Results using modelling of our deep JHK_s photometry combined with *Spitzer* photometry are described in §3. Properties of the newly discovered sources, estimation of sample contamination, and detailed comparisons with recently published deep, large-area NIR imaging surveys are contained in §4. The summary and conclusions are presented in §5.

2. Observations and Data Reduction

Observations of the ρ Ophiuchi cloud core were obtained during the period 2008 May 23 - 26 with the IRIS2 NIR imager/spectrograph on the Australian Astronomical Observatory's 4 m telescope (AAT). IRIS2 consists of a Hawaii HgCdTe 1024×1024 array which, when

mounted at the f/8 Cassegrain focus on the AAT, yields a plate scale of $0''.45 \text{ pixel}^{-1}$ with a corresponding field of view of approximately $7.7' \times 7.7'$. For all observations, the J , K_s (1.25 , $2.14 \mu\text{m}$), CH_{4s} ($1.59 \mu\text{m}$), and CH_{4l} ($1.673 \mu\text{m}$) filters were used. Details of our observation and data reduction procedures for all filters are discussed in Haisch, Barsony, & Tinney (2010). However, because this paper makes extensive use of the J and K_s data, which the previous work did not, we summarize below the observations and image reduction process for these filters.

Nineteen IRIS2 fields, centered at $\alpha = 16^h26^m56.34^s$, $\delta = -24^\circ28'52''.22$ (J2000), were observed in a rectangular pattern covering an area of $\sim 920 \text{ arcmin}^2$ on the sky. The observed area is shown by the solid outlines in Figure 1, superposed on the extinction map that was derived from the 2MASS catalog³ as part of the COMPLETE project (Ridge et al. 2006; Lombardi et al. 2008) using the NICER algorithm (Lombardi & Alves 2001). Each field was spatially overlapped by 1 arcminute in both right ascension and declination to allow for redundancy of photometric measurements of sources located in the overlapped regions. All fields were observed in the Mauna Kea Observatory (MKO) photometric system J and K_s filters in a five point dither pattern with $30''$ offsets between each dither. Integration times at each dither position for the J and K_s filters were $15 \text{ seconds} \times 4 \text{ coadds}$ and $6 \text{ seconds} \times 10 \text{ coadds}$, respectively, for a total integration time of 5 minutes in each filter. The FWHM for all observations varied between approximately $2.2 - 3.1 \text{ pixels}$ ($\sim 1''.0 - 1''.4$), with the worst seeing being at the shortest wavelengths (*e.g.*, the J filter).

All data were reduced using the Image Reduction and Analysis Facility (IRAF)⁴. An average dark frame was constructed from the dark frames taken at the beginning and end of each night's observations. This dark frame was subtracted from all target observations to yield dark subtracted images. Sky frames in each filter were individually made for each observation by median-combining all five J and K_s band frames for each field. The individual sky frames were normalized to produce flat fields for each target frame. All target frames were processed by subtracting the appropriate sky frames and dividing by the flat fields. Target frames were then registered and combined to produce the final reduced images in each filter. H -band images of each field were constructed by adding the corresponding CH_{4s} and CH_{4l} images for the particular field in question.

Infrared sources were identified at K_s -band using the automated source extractor DAOFIND

³http://www.cfa.harvard.edu/COMPLETE/data_html_pages/OphA_Extn2MASS_F.html

⁴IRAF is distributed by the National Optical Astronomy Observatories, which are operated by the Association of Universities for Research in Astronomy, Inc., under cooperative agreement with the National Science Foundation.

routine within IRAF (Stetson 1987). DAOFIND was run on each field using a FWHM of 2.8 pixels, and a single pixel finding threshold equal to 3 times the mean noise of each image. Each field was individually inspected, and the DAOFIND coordinate files were edited to remove bad pixels and any objects misidentified as stars, as well as to add any missed stars to the list. Objects within $30''$ of the field edges were also removed from the list, as they were in low signal to noise regions of the image as a result of the dither pattern used. Aperture photometry was then performed on all fields in each filter using the PHOT routine within IRAF. An aperture of 4 pixels in radius was used for all target photometry, and a 10 pixel radius was used for the standard star photometry. Sky values around each source were determined from the mode of intensities in an annulus with inner and outer radii of 10 and 20 pixels, respectively. Our choice of aperture size for our target photometry insured that the individual source fluxes were not contaminated by the flux from neighboring stars; however, they are not large enough to include all the flux from a given source. In order to account for this missing flux, aperture corrections were determined using the MKAPFILE routine within IRAF. The instrumental magnitudes for all sources were corrected to account for the missing flux.

Photometric calibration was accomplished using the list of standard stars of (Persson et al. 1998). The standards were observed on the same nights and through the same range of air masses as the ρ Ophiuchi cloud. Zero points and extinction coefficients were established for each night.⁵ All magnitudes and colors were transformed to the CIT system using MKO to 2MASS and 2MASS to CIT photometric color transformation equations⁶, and the conversion relations of Stephens & Leggett (2004). Because of the extensive spatial overlapping of the cloud images, a number of sources were observed at least twice. We compared the JHK_s magnitudes of 200 duplicate stars identified in the overlap regions. For all stars brighter than the completeness limit of our survey, the photometry of the duplicate stars agreed to within 0.15 magnitudes. Plots of our photometric errors as a function of magnitude are presented in Figure 2, for J (left panel), H (middle panel), and K_s (right panel).

The completeness limit of our observations was determined by adding artificial stars at random positions to each of the 19 fields in all four filters and counting the number of sources recovered by DAOFIND. Artificial stars were added in twelve separate half-magnitude bins, covering a magnitude range of 16.00 to 22.00, with each bin containing 100 stars. The artificial stars were examined to ensure that they had the same FWHM as the real sources in each image. Aperture photometry was performed on all sources to confirm that the assigned

⁵We found a zero point offset of 1.8 mag through each filter.

⁶See <http://www.astro.caltech.edu/~jmc/2mass/v3/transformations/>

magnitudes of the added sources agreed with those returned by PHOT. All photometry agreed to within 0.10 mag. DAOFIND and PHOT were then run and the number of identified artificial sources within each half-magnitude bin was tallied. This process was repeated 20 times. We estimate that our survey is 90% complete to $J = 20.00$, $H = 20.00$, and $K_s = 18.50$. Furthermore, saturation of objects in each image occurred at $J \simeq 12.0$, $H \simeq 11.0$, and $K_s \simeq 10.0$, respectively. Thus our observations are sensitive to $12.0 \leq J \leq 20.0$, $11.0 \leq H \leq 20.0$, and $10.0 \leq K_s \leq 18.5$, respectively.

Coordinates for all objects were determined relative to the positions of known objects in the 2MASS⁷ catalog. In particular, plate solutions were done using the 2MASS catalog in conjunction with WCSTools, a package of programs and a library of utility subroutines for setting and using the world coordinate system in the headers of the most common astronomical image formats to relate image pixels to sky coordinates.⁸ The resulting coordinates of all objects in our survey have typical rms uncertainties of $\sim 0''.20$ relative to the coordinates of previously known stars used in their determinations.

3. Results

We detected a total of 2283 sources at all three wavelengths at or brighter than our JHK_s completeness limits within the 920 arcmin² region outlined by the solid black lines in Figure 1. Of course, many more sources were detected at each individual waveband. At K_s , we detected 7081 sources to 5σ , and 6882 to our $K_s = 18.50$ completeness limit. We used the locations of the K_s detections to search for counterparts at H and J . Since we used the combination of the 30-min. on-source duration observations in the methane-on and methane-off filters to construct the H -band image, instead of just the 5 minutes total on-source integration times at K_s and J -bands, we detected 7090 sources at H to 5σ , and 6986 to our $H = 20.0$ completeness limit. Finally, we detected just 3486 sources to 5σ at J , and 2404 to our $J = 20.00$ completeness limit, reflecting the fact that we were observing through the highest extinction portions of the ρ Oph core.

Our survey boundaries are indicated in Figure 1, superposed on the extinction map (described in § 2), displayed in both greyscale and by contour levels. From Figure 1, it is

⁷This publication makes use of data products from the Two-Micron All-Sky Survey, which is a joint project of the University of Massachusetts and the Infrared Processing and Analysis Center/California Institute of Technology, funded by the National Aeronautics and Space Administration and the National Science Foundation.

⁸<http://tdc-www.harvard.edu/wcstools/>

evident that our survey encompassed the highest extinction portions of the ρ Oph cloud core. The vast majority of detected sources lie between the $A_V = 5$ and $A_V = 15$ contour levels, whereas much of the surveyed area has $A_V \geq 20$.

In Figure 3 (left panel), we present the $J - H$ vs. $H - K_s$ color-color diagram for all 2283 objects with $10 \leq K_s \leq 18.5$ in our survey area, with available photometry at all three (JHK_s) bands in our data. The greatest uncertainty in the colors is less than 0.2 magnitudes for all sources and is indicated by the size of the cross in each panel of Figure 3. The solid curve in each panel represents the locus of colors corresponding to unreddened main sequence stars, ranging in spectral type from early O to M9, after converting the 2MASS colors to the CIT system. The locus of the colors of giant stars is represented by a dashed line in each panel (Bessell & Brett 1988). The two parallel dashed lines define the reddening band for main sequence stars and are parallel to the reddening vector. The classical T Tauri star (CTTS) locus in these diagrams extends from $J - H = 0.81$, $H - K = 0.50$ to $J - H = 1.10$, $H - K_s = 1.00$ (Meyer, Calvet, & Hillenbrand 1997). A diagonal arrow representing the effect of 5 magnitudes of visual extinction is also shown. The reddening law of Cohen et al. (1981), derived in the CIT system and having a slope of 1.692, has been adopted.

Note the offset of the detected sources in the left panel of Figure 3 from the (0,0) position in the color-color diagram, indicating all sources suffer *at least* $A_V = 5$ mag of visual extinction—confirming that we are looking through the darkest portion of the ρ Oph cloud core. Of the 2283 stars plotted in the left panel of Figure 3, 1139 de-redden to the CTTS locus. Therefore, these objects possess infrared excess emission, and are referred to as “excess sources” in the following. Among the 1139 excess sources, 830 have available *Spitzer* photometry. We have divided the remaining sources into two groups. The first group consists of 709 “non-excess” sources—those which definitely would not de-redden to the CTTS locus. The second group, consisting of 435 sources, would de-redden to photospheric colors characteristic of very low-mass stars or brown dwarfs of spectral types in the range M7–L0 as given by Luhman et al. (2010). Of the 709 sources which do not display infrared excesses, 533 have available *Spitzer* photometry. Of the 435 sources which would de-redden to M7–L0 photospheric colors, 378 have available *Spitzer* photometry.

We have estimated the effective temperatures for the 1723 sources for which successful fits were obtained to both our JHK_s photometry and to the *Spitzer* mid-infrared photometry. *Spitzer* photometry is taken from either the c2d (the *Spitzer* “From Molecular Cores to Planet-Forming Disks” Legacy Program) CLOUDS catalog for L1688⁹ or, from Gutermuth et al. (2009), for sources not present in the c2d catalog.

⁹<http://irsa.ipac.caltech.edu/data/SPITZER/C2D/clouds.html>

The combined NIR and *Spitzer* photometry for each source was fit with a model spectrum to estimate its effective temperature, T_{eff} . Four possible models were used for each source. These were: *i)* the 1 MYr COND models for $T_{eff} \leq 1500K$ (Baraffe et al. 2003), *ii)* the 1 MYr DUSTY models for $1500K \leq T_{eff} \leq 3000K$ (Chabrier et al. 2000), *iii)* the NextGen models for $T_{eff} \geq 1700K$, with solar gravity and metallicity (Hauschildt, Allard, & Baron 1999), or *iv)* blackbody spectra for all possible temperatures. De-reddened K_s magnitudes (for $d = 124$ pc) were derived using the observed K_s magnitudes and the A_V estimates obtained by de-reddening each source to either the main-sequence (within the reddening band of Figure 3) or to the CTTS locus (for sources to the right of the reddening band of Figure 3). Figure 3 (right panel) shows the distribution of sources in the JHK_s color-color diagram which are found to lie above the main-sequence from our SED fits.

In Figure 4, we present the dereddened K_s magnitude as a function of estimated effective temperature for the 827 “excess” (top panel) and the 527 “non-excess” (middle panel) sources for which successful fits were obtained to their spectral energy distributions determined by our new JHK_s data combined with *Spitzer* data. Objects in the cloud-exterior region, from the same off-cloud region as in Marsh et al. (2010a), are plotted in the bottom panel of Figure 4, for comparison. This bottom panel shows the results of fits to 509 off-cloud sources for which both deep JHK_s and *Spitzer* photometry are available.

All three panels of Figure 4 show model curves for the 1 Myr COND (dashed) and DUSTY (dotted) models, and for main sequence stars (solid) for an assumed distance of 124 pc. The T_{eff} ranges used for the different atmospheric models are color-coded, and indicated at the bottom of each panel. Sources best-fit using the 1 MYr COND models are plotted in red, those best-fit using the 1 MYr DUSTY models are plotted in green, and those best-fit using the NextGen models are plotted in mustard. In addition, fits to blackbodies of a specified temperature are plotted in blue.

Details of the fitting procedure are described in Marsh et al. (2010a), with the improvement in the present work that the *Spitzer* filter bandpasses have been convolved with the model atmospheres to derive *Spitzer* IRAC magnitudes for each model. For purposes of the model-fitting described above, A_V values were assigned to be those derived from de-reddening each source to the classical T-Tauri (CTTS) locus of Figure 3, for the “EXCESS” sources, and those derived by de-reddening to the main-sequence for the “NON-EXCESS” sources, instead of letting A_V be a free parameter.

In order to test the validity of our fitting procedure, we plot the locations assigned by our SED-fitting program to known, spectroscopically confirmed, brown dwarfs in ρ Oph from the tabulation of Geers et al. (2011). In Figure 4, the open diamonds represent known brown dwarfs with IR excesses (top panel) and known brown dwarfs without IR excesses

(middle panel). In both cases, our fitting would independently determine these objects to lie above the main-sequence, and to have low values of T_{eff} .

4. Discussion

4.1. Candidate New Members and Their Properties

The identification of the new candidate cloud members in ρ Oph is primarily based on their location in the plots of Figure 4. The top panel of Figure 4 shows a dramatically different distribution of sources from those in the middle and bottom panels. Note the dearth of reddened main-sequence stars in the top panel combined with the presence of disks, inferred from the preponderance of blackbody best-fits. In the top panel of Figure 4, 764 of the 827 successfully fit infrared excess sources lie above the main sequence, identifying them as pre-main-sequence objects, and thus as candidate cluster members. The open diamonds plotted in the top panel of Figure 4 represent fits to the photometry of previously known and spectroscopically confirmed brown dwarf members of the cluster that also display infrared excess emission from disks, for comparison.

An artifact in the top panel of Figure 4 is the presence of a gap in the distribution of T_{eff} values from the model fits in the $1200\text{ K} \leq T_{eff} \leq 1800\text{ K}$ range. The root cause of this gap is that objects surrounded by circumstellar material, and, therefore, exhibiting spectral energy distributions (SEDs) characteristic of disks or late-stage protostars, were fit to purely photospheric models (COND, DUSTY, NextGen, Blackbody). At the lowest temperatures ($T_{eff} \leq 1500\text{ K}$), the COND models tend to give fairly flat-looking SEDs which often provide artificially good fits to flat spectrum protostars, while the more evolved young stellar objects are better fit by higher-temperature models which are more Planck-like (DUSTY, NextGen, Blackbody). It can be seen from the top panel of Figure 4 that the distinct gap in the distribution of sources in the $1200\text{ K} \leq T_{eff} \leq 1800\text{ K}$ range is not an artifact of the 1500 K boundary between the COND and DUSTY models – rather, this gap represents the temperature range over which none of the photospheric models can adequately mimic circumstellar disks.

A substantial fraction of the newly discovered population of “excess” sources plotted in the top panel of Figure 4 seems concentrated above the lowest T_{eff} NextGen models, but below the COND/DUSTY models. This is very likely due to suppressed K-band flux due to extinction of the YSO photospheres by cool disk material (e.g., Mayne & Harries 2010).

In the middle panel of Figure 4, we plot the 527 “non-excess” sources for which successful SED fits were obtained to our combined JHK_s and available *Spitzer* photometry. Among

these “non-excess” sources, most (343/527) lie in the region below the main-sequence at the cloud’s distance in the de-reddened K_s vs. T_{eff} plot. Therefore, most of the non-excess sources are consistent with being background objects. However, 184 of the 527 non-excess sources plotted in the middle panel of Figure 4 lie above the main-sequence, and are candidate cloud members. The open diamonds plotted in the middle panel of Figure 4 show the locations of fits to the photometry of previously known, spectroscopically confirmed, brown dwarf members of the cluster, that lack infrared excess emission.

The bottom panel of Figure 4 shows the distribution of sources from an off-cloud region (same off-cloud region as used by Marsh et al. 2010a, to 5σ detection limits of $J = 20.5$, $H = 20.0$, and $K_s = 19.0$). The majority of objects detected in the off-cloud region lie below the locus of main-sequence photospheres at the distance to ρ Oph. Sources falling below the main-sequence locus in Figure 4 are reddened background stars.

We therefore find a total of 948 candidate young stellar objects (YSOs) in the ρ Ophiuchi cluster, of which 764 are excess sources, and 184 are non-excess sources. Table 3 lists these sources. Column 1 of Table 3 is an ordinal source identification number, followed by each candidate object’s $\alpha(2000)$ and $\delta(2000)$ coordinates. We then list our near-infrared photometry in the order, J , σ_J , H , σ_H , K_s , σ_{K_s} , followed by the IRAC photometry with corresponding errors in each of the four IRAC bands ($3.6 \mu\text{m}$, $4.5 \mu\text{m}$, $5.8 \mu\text{m}$, and $8.0 \mu\text{m}$, respectively) in ascending wavelength order. The next column lists the extinction values (A_V) derived by de-reddening each source to either the main-sequence (for “non-excess” sources) or to the CTTS locus (for “excess” sources) in the $J - H$ vs. $H - K_s$ color-color diagram of Figure 3. The next column lists the best-fit value of T_{eff} derived from model fitting to the SED of each source. The penultimate column lists the best-fit model type used to derive the tabulated T_{eff} value. The last column indicates whether an individual source is an “excess” source (E) or “non-excess” source (NE).

The right panel of Figure 3 shows a plot of the location of these 948 candidate cluster members in the $J - H$ vs. $H - K_s$ color-color diagram. A large fraction, 764/948 or 81%, of our candidate members lie in the infrared excess region of the JHK_s color-color diagram in Figure 3. Predictions from both observations and modeling suggest that this is what one would expect for excess emission from circumstellar disks (e.g., Lada & Adams 1992; Meyer, Calvet, & Hillenbrand 1997; Haisch et al. 2000). If the infrared excesses do indeed originate in circumstellar disks, then this strengthens their identification as a significant population of new low mass YSOs in the ρ Ophiuchi cloud.

Figure 5 shows fit results for the subset of the 435 sources which could be de-reddened to very low-mass stellar or brown dwarf colors in the $J - H$ vs. $H - K_s$ color-color diagram of Figure 3, for which good SED fits could be obtained. The three panels of Figure 5 illustrate

the fact that, for this sample, the fraction of objects inferred to be pre-main-sequence, and, therefore, to be potential cluster members, varies greatly with their assumed, intrinsic, unreddened colors, or, equivalently, with their derived values of A_v . For these new fits, the *a priori* values of extinction were based on de-reddening sources to the photospheric JHK_s colors given for the indicated intrinsic spectral type by Luhman *et al.* (2010) in the $J - H$ vs. $H - K_s$ diagram. *Spitzer* photometry was available for 378 of these 435 sources, and successful fits were obtained for 373 (top panel), 368 (middle panel), and 372 (bottom panel) sources. The top panel shows the results of assuming an intrinsic spectral type of M7 for all fitted sources. In this case, only 81/373 fitted sources would be inferred to lie above the main-sequence. The middle panel shows the results of assuming an intrinsic spectral type of L0 for all fitted sources. In this case, 348/368 fitted sources would be inferred to lie above the main-sequence. Finally, the bottom panel shows the results of assuming an intrinsic spectral type somewhere between M7 and L0, close to M9. In this case, 312/372 well-fit sources would be inferred to lie above the main-sequence. Due to this large variation in the inferred fraction of pre-main-sequence sources depending on the assumed intrinsic spectral type of each source for sources lying in this narrow range of the $J - H$ vs. $H - K_s$ color-color diagram, we do not yet include any of these among the new, low-mass, YSO population of ρ Oph. Follow-up spectroscopy will reveal the intrinsic spectral types of this subset of objects, and will determine what fraction are cloud members.

For our 948 candidate cloud members, however, we can estimate the range of masses to which this survey is potentially sensitive, given the distribution of JHK_s brightnesses. At the low mass end, our JHK_s survey is sensitive to a bare photosphere with $T_{eff} \sim 1100$ K for the 1 MYr COND models at the distance to ρ Oph, with no reddening, corresponding to $\sim 1.5 M_{Jup}$. This rises to 2.0, 4.0, and 8.5 M_{Jup} for $A_V = 5, 10$, and 15, respectively. At the high mass end, a source with $K_s \sim 14.0$ corresponds to an absolute K_s of 8.52 or a $T_{eff} \sim 2250$ K – which is a late M spectral type. This K_s magnitude corresponds to a mass of 10 M_{Jup} for the 1 MYr COND model, and rises to 15, 35, and 45 M_{Jup} for $A_V = 5, 10$, and 15, respectively. However, these estimates do not take the complicating factor of disk excesses into account. Spectroscopic follow-up is required to confirm the nature of individual objects, and to better constrain their parameters. Because spectra for our candidate members are not available, it is not currently possible to derive a meaningful IMF for these objects. Nevertheless, the potential to determine the IMF for this cluster from $\sim 2 M_{Jup}$ through the substellar boundary is now a step closer.

4.2. Contamination

4.2.1. Extragalactic

We have completed a deep, wide-field, near-infrared imaging survey of the ρ Ophiuchi cloud core to search for candidate low mass member YSOs. Establishing membership of a given YSO in a star-forming region generally requires multi-wavelength observations, since multiple indicators of youth are required to establish membership for any individual candidate source. The candidate YSOs we have identified were selected based on fits to broad-band spectral energy distribution (SEDs). Many of our candidate objects display infrared excess emission, generally a good indicator of youth. Infrared excess, by itself, however, may not always be definitive to establish membership of an individual source, since background active galactic nuclei (AGN) could mimic YSO colors. However, given the high extinction region to which our observations were limited, the effects of contamination by background galaxies, AGN, or red giants are minimized, as demonstrated below.

An upper limit to the number of extragalactic contaminants among our candidate members can be obtained by contrasting the K_s vs. T_{eff} plots for sources projected within the cloud core in Figure 1 (the “cloud” region), with those sources in the cloud “exterior” region. Here, the “exterior” region is the same one as defined in Marsh et al. (2010a). Using the list of spectroscopically confirmed brown dwarfs from Geers et al. (2011) as a guide for the location of cloud members in the de-reddened K_s vs. T_{eff} plot, and assuming that all of the inferred cluster members in the cloud “exterior” region in such a plot are spurious, an estimate of the (largest possible) number of extragalactic contaminants can be made in the following manner.

The number of objects which fall below the main sequence in the K_s vs. T_{eff} plots of Figure 4 and are thus identified as background stars, in the “cloud” (including the “excess” and “non-excess” sources) region is 404, whereas the corresponding number in the cloud “exterior” region is 385. The number of sources above the main sequence in the “cloud” and “exterior” regions are 948 and 63, respectively. The number of contaminating sources in the “cloud” region can be predicted by scaling the number of “exterior” region objects that are above the main sequence (63) by the cloud:exterior background source count ratio, which is equal to 1.05 from the background source counts estimated above (404/385). Because background source counts are heavily affected by extinction, it is not appropriate to scale by the relative areas of the two regions. Rather, the scaling must be based on the number density ratio of extragalactic sources to background stars, which is the same for the “cloud” and “exterior” regions. Multiplying our cloud:exterior background source count ratio (1.05) by the exterior:cloud PMS source ratio (63/948), we find an upper limit to the percentage

of contaminating sources among our candidate members of $\sim 7\%$. Thus, 66 of our 948 candidate YSOs could be extragalactic background objects.

An alternative approach to estimating background contamination by extragalactic sources may be derived by inspection of Figure 6, in which we plot the JHK colors of galaxies in the GOODS (Great Observatories Origins Deep Survey)-South field imaged with VLT-ISAAC, after transforming the $J-H$ and $H-K_s$ colors to the CIT system. This makes Figure 6 directly comparable to Figure 3. The NIR GOODS-S data were acquired over a ~ 160 arcmin² region (Retzlaff et al. 2010). The total number of galaxies is 76 in this field to our completeness limits. The GOODS-S field was observed through negligible extinction, whereas the *minimum* extinction towards our 920 arcmin² region is $A_v = 5$ (see text regarding Figure 3 in §3, the Results section). Therefore, in Figure 6 we present plots of the appearance of the same 76 galaxies as if they were observed through $A_v = 5$ (grey filled circles) and $A_v = 10$ (black filled circles). Increasing the extinction has the dual effect of reddening and dimming these sources, such that only 42 galaxies and 22 galaxies, respectively, would be detected to our completion limits seen through $A_v = 5$ and $A_v = 10$. More importantly, the general population of background galaxies at these faint NIR magnitudes have very blue colors, so that they would not contaminate the “excess” region of the JHK_s color-color plot.

4.2.2. Galactic

Red giants and faint red dwarfs are expected to be the major source of Galactic contaminants to our sample of candidate new, low-mass members of the ρ Oph YSO population. Such contamination is minimized given the high extinction over most of our survey area, combined with its relatively high galactic latitude ($16.377799^\circ \leq b \leq 17.153386^\circ$).

An excellent estimate of Galactic contamination can be made directly from our modeling efforts. Of the 2283 total sources detected to our JHK_s completeness limits, 1741 (including 830 “excess” and 530 “non-excess”) sources have available *Spitzer* photometry. Of these, 827 “excess” and 527 “non-excess” sources could be successfully fit. Of the 827 successfully fit “excess” sources, plotted in the top panel of Figure 4, 61 fall below the main-sequence locus for an assumed distance of 124 pc, whereas of the 527 successfully fit “non-excess” sources, plotted in the middle panel of Figure 4, 343 fall below the main-sequence. Thus, the total number of objects falling below the main-sequence from our fits is 404. This is our estimate of the number of Galactic background stars amongst the objects for which good fits to our JHK_s and *Spitzer* photometry could be made. These Galactic contaminants are not counted amongst our 948 candidate YSOs.

4.3. Comparison with Other Surveys

A total of 316 verified (or candidate) members of the ρ Ophiuchi cloud are listed in a recent review article (Willing et al. 2008). Of these, 219 lie within our survey boundaries, and only 28 have $K_s \geq 14$. Of the 219 objects lying within our survey boundaries, 70 are saturated in our data at K_s band, and a further 40 are undetected in our J band data. This leaves 109 targets for which we have full JHK_s and *Spitzer* IRAC photometry. All 109 were fit with our model-fitting algorithm, and 87 were found to lie above the main-sequence. Of these 87 pre-main-sequence sources, 57 lie in the “excess” region of the $J - H$ vs. $H - K_s$ diagram, and 30 are in the “non-excess” region. This result demonstrates the efficacy of our modelling method at identifying pre-main-sequence objects in an unbiased fashion, with regard to the presence or absence of disks.

Spitzer-selected objects, without available corresponding deep NIR photometry, are necessarily biased towards identifying sources with disks, often necessitating follow-up with X-ray telescopes to identify the “missing” disk-less populations (e.g., Barrado et al. 2011; Pillitteri et al. 2010; Winston et al. 2010). Assuming the availability of sufficiently deep NIR and mid-IR photometry, our method presents an alternative approach to identifying the disk-less population in nearby star-forming regions. *This method also provides, for the first time, a uniform, unbiased means for identifying the entire pre-main-sequence population in these regions, in a statistical sense.*

Of course, selection biases are inherent in any observational effort—the aim is to understand what inherent biases there may be and to minimize their effect. Clearly, our method would not detect the two known Class 0 objects (VLA1623 and IRAS 16253–2429) in L1688. Very faint, nearly edge-on disk systems might also be missed, due to lack of detection at J -band. Nevertheless, the efficacy of this method for detecting a heretofore undiscovered, significant new pre-main-sequence population has been demonstrated, and the application of this method for uncovering new populations in other nearby star-forming regions is ongoing. Quantitative evaluation of selection biases inherent in this method, vis-a-vis evolutionary stage, source orientation, and degree of embeddedness in the cloud awaits future work.

A comparison of our JHK photometry with published photometry from the three recent, deep NIR surveys of ρ Oph is presented in Table 4. The coordinates of each source are listed first (as determined from our astrometry, described in §2 above), followed by our JHK_s photometry. The next set of columns display Alves de Oliveira et al’s (2010) source identifications and JHK_s photometry for sources in common with our survey (from their Table 4). The next set of columns display Marsh et al’s (2010a) source identifications and JHK_s photometry for sources in common with our survey (from their Table 1). Finally, the last 3 columns of Table 4 display Geers et al’s (2011) source identifications and JK_s

photometry for sources in common with our survey (from their Tables 1 & 2). Graphical presentations of these photometric comparisons are displayed in Figure 7.

Alves de Oliveira et al. (2010) list 110 candidate sub-stellar objects, of which 74 fell within our survey area. We list photometry for all but two of these (their Source 16, which fell on bad pixels, and their Source 72, which lies on a bright diffraction spike in our images). The photometric agreement between the two datasets is generally good (see top left column of Figure 7), with only Source 30 exhibiting highly discrepant values.

There are only 8 sources in common between Alves de Oliveira’s Table 4 and Marsh et al’s Table 1. These correspond with Marsh et al’s source nos. 829, 311, 654, 2978, 313, 222, 239, and 334. The root mean square error between the two sets of photometry for these sources, excluding Source 2978, is within 0.18 magnitudes at J , 0.12 magnitudes at H , and 0.090 magnitudes at K_s . For Marsh et al’s Source 2978, the magnitude differences between the two sets of photometry are 2.66 at J , 0.90 at H , and 0.21 at K_s , with Alves de Oliveira’s values always fainter. For the same source, our photometry varies from Marsh et al’s by 0.29 at H and 0.08 at K_s , with our values being the fainter ones (this source was not detected in our data at J). This photometric discrepancy may be due to the presence of extended faint nebulosity surrounding this object, as elaborated in the following for the case of the spectroscopically confirmed planetary mass object, Marsh et al’s Object 4450 (Marsh et al. 2010b).

For the seven candidate planetary mass objects for which spectra were obtained by Marsh et al. (2010b), Alves de Oliveira state they found good agreement (between 0.02 and 0.23 magnitudes difference) between the two sets of photometry at K_s for Marsh et al’s source nos. 1449, 1307, 2438, and 2403, but differences of 0.4, 1.42, and 1.47 magnitudes at K_s -band for Marsh et al’s source nos. 2974, 4450, and 3117, respectively. Unfortunately, Alves de Oliveira et al. did not publish the actual values for their JHK_s magnitudes for any of these sources, except for the J and K_s values for the spectroscopically confirmed planetary mass object, Object 4450. Our K_s photometry agrees with that of Marsh et al. within 0.1 mag for Source 1307, within 0.21 mag for Source 2438, and within 0.02 mag for source 2403, in agreement with Alves de Oliveira’s stated range of magnitude differences for these sources. Our K_s value for Object 4450 is 18.15, 0.44 fainter than Marsh et al’s K_s value of 17.71, but 1.01 magnitudes brighter than Alves de Oliveira’s K_s value of 19.14. Alves de Oliveira et al. could not derive an H -band value for Object 4450, due to an image artifact in their data. We derive $H=18.76$ compared with Marsh et al’s value of $H=18.36$. We did not detect Object 4450 at J band, whereas Marsh et al. derived $J=19.57$ and Alves de Oliveira derived $J=21.32 \pm 0.35$. Based on the large discrepancy between their K_s band value from Marsh et al’s for Object 4450, Alves de Oliveira et al. suggest that this planetary

mass object lies as far as the Sco-Cen association, and is not associated with the ρ Oph cloud. Our results do not support this conclusion.

There is a possible scenario that would resolve the issue of such large photometric discrepancies being reported by different workers for the planetary mass Object 4450. Note that the observed large differences in photometry between Marsh et al. and Alves de Oliveira et al. occur for 4/15 sources, suggesting the presence of a systematic, rather than random measurement error. One possibility is that of extended emission surrounding the objects with discrepant photometry, which we argue to be the case for Object 4450. The pixel size of 2MASS was $2''$ (used for the Marsh et al. photometry); the pixel size reported in this work was $0.45''$ (albeit in $1.0\text{--}1.4''$ seeing), and the pixel size for the CFHT WIRCam observations was $0.3''$, in excellent seeing, “typically between $0.4''\text{--}0.5''$ ”, but always better than $0.8''$. Alves de Oliveira used PSF-fitting photometry, which would miss measuring any extended flux, and would result in fainter measured magnitudes than would be derived for an extended object from aperture photometry. The hypothesis of an extended source is supported by our measurements falling between the values found by Alves de Oliveira on the one hand, and Marsh et al. on the other.

Of the 165 sources listed in Table 1 of Marsh et al. (2010a), photometry for 92 are listed in Table 4. Of the 73 sources not listed in Table 4, 50 are outside of our survey area, 20 are saturated in our data and 3 are below our detection threshold. The general photometric agreement between the two datasets is satisfactory and is plotted in the middle column of Figure 7.

Geers et al. (2011) list 36¹⁰ “likely substellar members with disks” in ρ Oph in their Table 1, of which 10 have NIR photometry from MOIRCS and 27 have NIR photometry from 2MASS. They list a further three “Probable Low-Mass and Substellar Members of ρ Oph with MOIRCS Spectroscopy Follow-up” in their Table 2. We recover all but four sources of which three (their Table 1 entries 11, 15, and 27) were outside of our survey limits, and one (their Table 1, entry 10) which was too faint at J to be detected by our survey, and is located in regions of very bad signal to noise in our survey at H and K . The photometric agreement between our surveys at J and K_s (no H band data were acquired by Geers et al. (2011)) is quite good as can be seen from the plots in the right column of Figure 7.

Recently, Geers et al. (2011) have estimated an upper limit for the ratio of low-mass stars ($0.1 M_{\odot} \leq M \leq 1.0 M_{\odot}$) to brown dwarfs ($M \leq 0.1 M_{\odot}$) in the ρ Ophiuchi cloud to be $\sim 3 - 7$. An alternative upper limit to the low-mass star: brown dwarf ratio in ρ Oph can be derived using the subsample of “non-excess” sources lying above the main-sequence (as

¹⁰Entries 8 and 24 in Table 1 of Geers et al. (2011) are identical.

plotted in the middle panel of Figure 4).

Only the “non-excess” sources whose SED fits had fluxes within a factor of 3 of what a photospheric model would predict at the distance of ρ Oph are considered, in order to exclude YSOs with non-photospheric mid-IR emission that might masquerade as having low-temperature photospheres (see discussion of this point in §4.1). Mass estimates for these sources are derived from their best-fit, 1MYr COND and DUSTY models, yielding 59 objects with masses in the range $0.1 \leq M \leq 1.0 M_{\odot}$, and 83 objects with $M \leq 0.1 M_{\odot}$, thus yielding a value of ~ 0.7 for the low-mass star: brown dwarf ratio. However, unaccounted for systematic biases (*e.g.*, under-estimating the number of higher-mass PMS sources) may have entered into this estimate. The point is to illustrate the variation in the possible range of this value in ρ Oph, given the present data. Marsh et al. (2010a) have recently published an estimate of the IMF in the ρ Ophiuchi cloud. Their results show an increase in the number of cloud members progressing from $0.1 M_{\odot}$ to lower masses. Our results, so far, are consistent with theirs. However, it would be premature to derive a definitive IMF across the substellar boundary from the data presented here. Future spectroscopy of our candidate cloud members will allow the construction of an IMF for this region, and further refine the value for the low-mass star: brown dwarf ratio in ρ Ophiuchi.

5. Summary and Conclusions

- We present a new, deep, JHK_s survey of a 920 arcmin² area of the ρ Ophiuchi star-forming cloud, encompassing its highest extinction core to 90% completeness limits of $J = 20.0$, $H = 20.0$, and $K_s = 18.50$. Our survey is thus sensitive to an object of just $\sim 1.5 M_{Jup}$ with an age of 1 MYr and photospheric temperature of ~ 1100 K at the distance to ρ Oph. This mass sensitivity falls to 2.0, 4.0, and $8.5 M_{Jup}$ for $A_V = 5$, 10, and 15, respectively.
- We combine our new, deep, JHK_s photometry with mid-infrared *Spitzer* photometry to produce SEDs for a total of 1741 sources within our survey boundaries. These sources are divided into three groupings according to their placement in the $J - H$ vs. $H - K_s$ color-color diagram into: *i*) 830 “excess” sources, those which de-redden to the CTTS locus of Meyer, Calvet, & Hillenbrand (1997); *ii*) 533 “non-excess” sources, which fall within the main-sequence reddening band, and *iii*) 378 sources that can be de-reddened to the colors of M7–L0 spectral types with a resulting large variation in their deduced extinction values.
- An improved version of the fitting procedure of Marsh et al. (2010a) is used to fit atmospheric models (COND, DUSTY, NextGen) and single-temperature blackbody

spectra to the observed SEDs for an age of 1 MYr and a distance of 124 pc, appropriate for the age and distance of the ρ Oph cloud’s YSO population.

- Of the 827 successful SED fits for “excess” sources, 764 are found to lie above the main-sequence. Of the 527 successful SED fits for “non-excess” sources, 184 lie above the main-sequence. We therefore identify 948 candidate pre-main-sequence sources, of which 87 (57 “excess” and 30 “non-excess”) are duplicates with sources listed in Wilking et al. (2008).
- The fact that 184 “non-excess” and 764 “excess” sources are identified as pre-main-sequence demonstrates the efficacy of this method for identifying the entire pre-main-sequence population in the surveyed area, unbiased with respect to the presence or absence of disks.
- Of the 378 sources with complete JHK_s and *Spitzer* SEDs that can be de-reddened to the colors of M7–L0 photospheres in the $J - H$ vs. $H - K_s$ color-color diagram, the fraction above the main-sequence varies from 22% (82 above main-sequence/374 successful SED fits) if all such sources are de-reddened to M7 colors, to 95% (357/377) if all such sources are de-reddened to L0 colors, and 78% (294/377) for sources de-reddened to colors that are the average between M7 and L0 colors (close to M9, in practice). Follow-up spectroscopy is required to decide what fraction of this sample represents further augmentation of the pre-main-sequence population of the cloud, and what fraction are reddened background stars.
- The embedded population of candidate YSOs in the ρ Oph core is increased by a factor of ~ 4 by this study, even allowing for contamination of the cluster member candidate sample by background galaxies or AGN.
- Follow-up spectroscopy of the cluster member candidates opens up the possibility for determination of the IMF in this star-forming cloud throughout the brown dwarf mass range, reaching well into the planetary mass regime.

We thank the AAO staff for their outstanding support in making our observations possible. We also thank Utah Valley University undergraduate physics student, Sherene Higley, for her assistance in the reduction of the AAO data. M.B., K.H., and C.M. acknowledge the support of NSF Research at Undergraduate Institutions grants AST-1007928, AST-1009776, and AST-1009590, respectively, for support of this research. M. B. gratefully acknowledges NSF grant AST-0206146 which made further contributions to this work possible. Additional support for this work was provided by the National Aeronautics and Space Administration

through Chandra Award Number AR1-2005A and AR1-2005B issued by the Chandra X-Ray Observatory Center, which is operated by the Smithsonian Astrophysical Observatory for and on behalf of NASA under Contract NAS8-39073.

REFERENCES

- Alves de Oliveira, C., Moraux, E., Bouvier, J., Bouy, H., Marmo, C., & Albert, L. 2010, *A&A*, 515, 75
- Andersen, M., Meyer, M.R., Greissl, J., & A. Aversa 2008, *ApJ*, 683, L183
- Baraffe, I., Chabrier, G., Barman, T.S., Allard, F., & Hauschildt, P.H. 2003, *A&A*, 402, 701
- Barsony, M., Ressler, M.E., & Marsh, K.A. 2005, *ApJ*, 630, 381
- Barrado, D., Stelzer, B., Morales-Calderón, M., Bayo, A., Huélamo, N., Stauffer, J.R., Hodgkin, S., Galindo, F., & E. Verdugo 2011, *A&A*, 526, 21
- Bessell, M.S., & Brett, J.M. 1988, *PASP*, 100, 1134
- Bihain, G. et al. 2009, *A&A*, 506, 1169
- Burgess, A.S.M., Moraux, E., Bouvier, J., Marmo, C., Albert, L., & Bouy, H. 2009, *A&A*, 508, 823
- Caballero, J.A. et al. 2007, *A&A*, 470, 903
- Chabrier G., Baraffe, I., Allard, F., & Hauschildt, P.H. 2000, *ApJ*, 542, 464
- Cohen, J.G., Frogel, J.A., Persson, S.E., & Elias, J.H. 1981, *ApJ*, 249, 481
- Cómeron, F. 2011, *A&A*, 531, 33
- Geers, V., Scholz, A., Jayawardhana, R., Lee, E., Lafrenière, D., & Tamura, M. 2011, *ApJ*, 726, 23
- Gutermuth, R.A., Megeath, S.T., Myers, P.C., Allen, L.E., Pipher, J.L., & Fazio, G.G. 2009, *ApJS*, 184, 18
- Hauschildt, P.H., Allard, F., & Baron, E. 1999, *ApJ*, 512, 377
- Haisch Jr., K.E., Barsony, M., & Tinney, C. 2010, *ApJ*, 719, L90
- Haisch Jr., K.E., Lada, E.A., & Lada, C.J. 2000, *AJ*, 120, 1396

- Hennebelle, P. & Chabrier, G. 2011, IAU Symp. 270, pp.159-168
- Kroupa, P. 2011, IAU Symp. 270, pp.141-149
- Lada, C.J., & Adams, F.C. 1992, ApJ, 393, 278
- Lodieu, N., Zapatero Osorio, M.R., Rebolo, R., Martín, E.L., & N.C. Hambly 2009, A&A, 505, 1115
- Loinard, L., Torres, R.M., Mioduszewski, A., & Rodriguez, L.F. 2008, ApJ, 675, L29
- Lombardi, M., Lada, C.J., & Alves, J. 2008, A&A, 489, 143
- Lombardi, M. & J. Alves 2001, A&A, 377, 1023
- Luhman, K.L. & Rieke, G.H. 1999, ApJ, 525, 440
- Luhman, K.L., Stauffer, J.R., Muench, A.A., Rieke, G.H., Lada, E.A., Bouvier, J., & Lada, C.J. 2003, ApJ, 593, 1093
- Luhman, K.L. 2004, ApJ, 617, 1216
- Luhman, K.L., Whitney, B.A., Meade, M.R., Babler, B.L., Indebetouw, R., Bracker, S., & E.B. Churchwell 2006, ApJ, 647, 1180
- Luhman, K.L. 2007, ApJS, 173, 104
- Luhman, K.L., Mamajek, E.E., Allen, P.R., Muench, A.A., & D.P. Finkbeiner, 2009a, ApJ, 691, 1265
- Luhman, K.L., Mamajek, E.E., Allen, P.R., & Cruz, K.L. 2009b, ApJ, 703, 399
- Luhman, K.L., Allen, P.R., Espaillat, C., Hartmann, L., & L. Calvet 2010, ApJS, 186, 111
- Marsh, K.A., Plavchan, P., Kirkpatrick, J.D., Lowrance, P.J., Cutri, R.M., & Velusamy, T. 2010a, ApJ, 719, 550
- Marsh, K.A., Kirkpatrick, J.D., & Plavchan, P. 2010b, ApJ, 709, L158
- Mayne, N.J. & Harries, T.J. 2010, MNRAS, 409, 1307
- McKee, C. & Ostriker, E. 2007, ARA&A, 45, 565
- Meyer, M.R., Calvet, N., & Hillenbrand, L.A. 1997, AJ, 114, 288
- Monin, J.-L. et al. 2010, A&A, 515, 91

- Muench, A.A., et al. 2003, AJ, 125, 2029
- Muench, A.A., Lada, E.A., & Alves, J. 2002, ApJ, 573, 366
- Mužić, K., Scholz, A., Geers, V., Fissel, L., & R. Jayawardhana 2011, ApJ, 732, 86
- Persson, S.E., Murphy, D.C., Krzeminski, W., Roth, M., & Rieke, M.J. 1998, AJ, 116, 2475
- Pillitteri, I., Sciortino, S., Flaccomio, E., Stelzer, B., Micela, G., Damiani, F., Testi, L., Montmerle, T., Grosso, N., Favata, F., & G. Giardino 2010, A&A, 519, 34
- Prato, L., Greene, T.P., & Simon, M. 2003, ApJ, 584, 853
- Preibisch, T., Stanke, T., & Zinnecker, H. 2003, A&A, 409, 147
- Rebull, L.M. et al. 2010, ApJS, 186, 259
- Retzlaff, J., Rosati, P., Dickison, M., Vandame, B., Rit  , C., Nonino, M., Cesarsky, C., and the GOODS Team 2010, A&A, 511, 50
- Riaz, B. & Mart  n, E.L. 2011, A&A, 525A, 10
- Ridge, N. et al. 2006, AJ, 131, 2921
- Robberto, M., Soderblom, D.R., Scandariato, G., Smith, K., Da Rio, N., Pagano, I., & L. Spezzi 2010, AJ, 139, 950
- Scholz, A., Geers, V., Jayawardhana, R., Fissel, L., Lee, E., Lafreniere, D., & Tamura, M. 2009, ApJ, 702, 805
- Slesnick, C.L., Hillenbrand, L.A., & Carpenter, J.M. 2004, ApJ, 610, 1045
- Stephens, D.C., & Leggett, S.K. 2004, PASP, 116, 9
- Stetson, P. 1987, PASP, 99, 191
- Terebey, S., van Buren, D., Padgett, D.L., Hancock, T., & M. Brundage 1998, ApJ, 507, L71
- Todorov, K., Luhman, K.L., & McLeod, K.K. 2010, ApJ, 714, L84
- Weights, D.J., Lucas, P., Roche, P.F., Pinfield, D.J., & Riddick, F. 2009, MNRAS, 392, 817
- Willing, B.A., Meyer, M.R., Robinson, J.G., & Greene, T.P. 2005, AJ, 130, 1733

- Wiling, B.A., Gagné, M., & Allen, L.E. 2008, *Handbook of Star Forming Regions, Vol. II, The Southern Sky*, ASP Monograph Publications, Vol. 5, ed. B. Reipurth, p.351
- Winston, E., Megeath, S.T., Wolk, S.J., Spitzbart, B., Gutermuth, R., Allen, L.E., Hernandez, J., Covey, K., Muzzerolle, J., Hora, J.L., Myers, P.C., & G.G. Fazio 2010, AJ, 140, 266

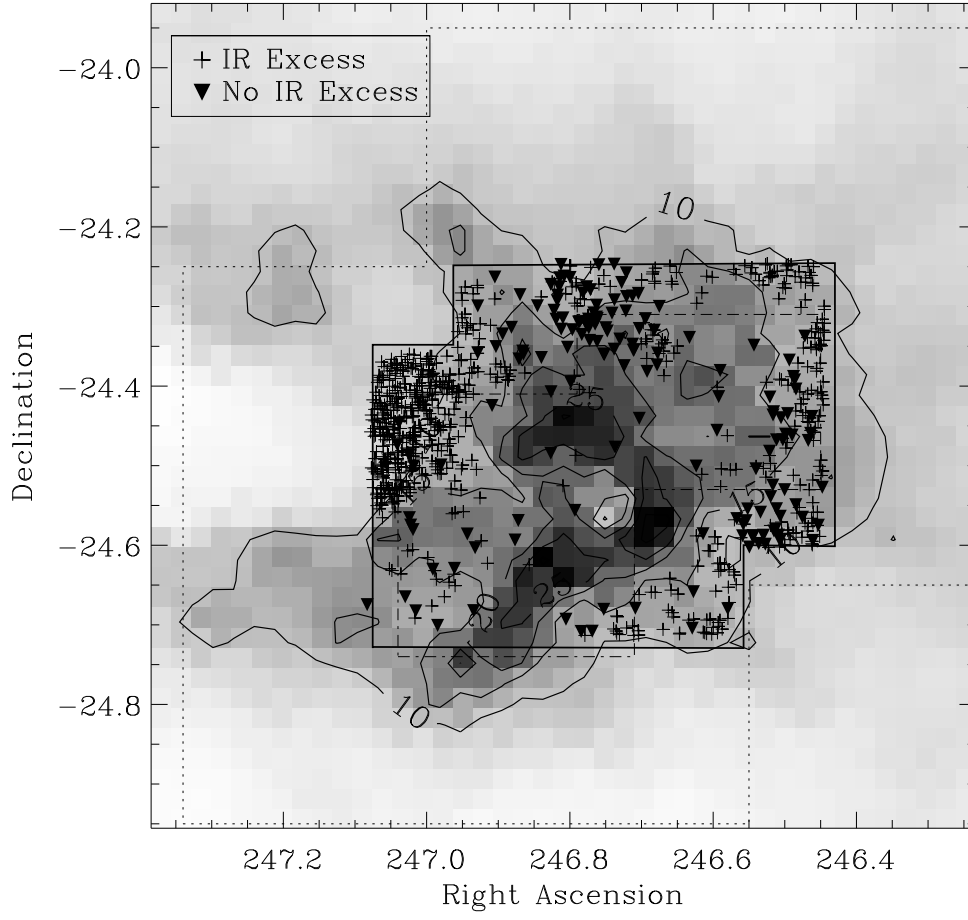


Fig. 1.— Plot of spatial distribution of our candidate ρ Oph members (crosses=excess sources, filled triangles=non-excess sources) superposed on the A_V contours from the COMPLETE project. A_V contours are plotted and labelled at $A_V = 10, 15, 20$, and 25 . Our 920 arcmin^2 survey area is indicated by the solid outline. The survey areas of Geers et al. and Alves de Oliveira et al. are indicated by the dot-dashed and dotted outlines, respectively.

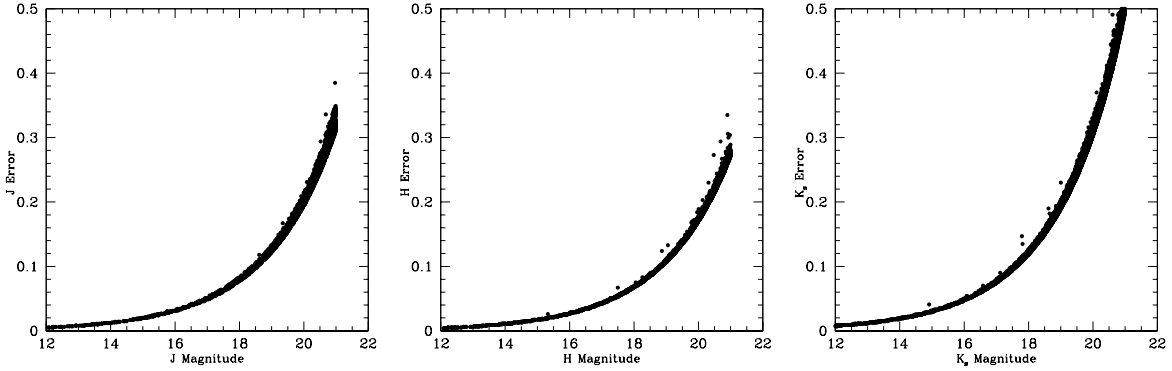


Fig. 2.— Photometric errors as a function of magnitude at J (left panel), H (middle panel), and K_s (right panel). Completeness limits are at $J = 20.0$, $H = 20.0$, and $K_s = 18.50$, as discussed in the text. Saturation limits are at $J \simeq 12.0$, $H \simeq 11.0$, and $K_s \simeq 10.0$.

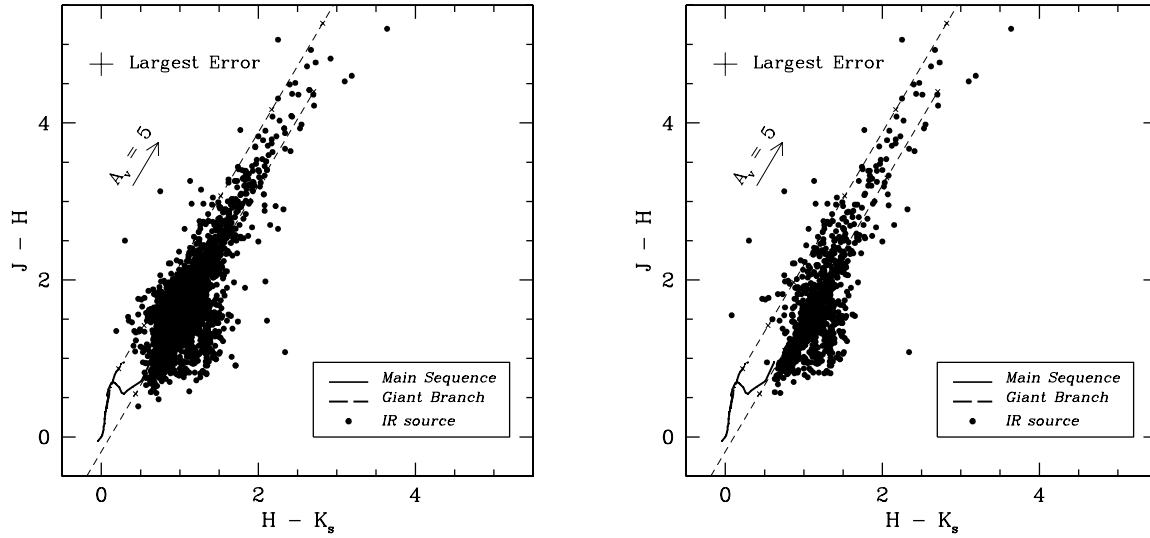


Fig. 3.— JHK_s color-color diagrams for sources with $10 \leq K_s \leq 18.5$ detected in all 3 bands in our survey of ρ Oph (*left*), and for all objects falling above the main-sequence after SED-fitting (see text) (*right*). In the diagrams, the solid line represents the locus of points corresponding to the unreddened main sequence, continuing into the realm of cool young photospheres. The dashed diagonal lines indicate the main-sequence reddening band. The locus of positions of giant stars is shown as a heavy dashed line. The CTTS locus (not plotted) extends from $[0.81, 0.50] \leq [J - H, H - K] \leq [1.10, 1.00]$. The diagonal arrow represents the effect of 5 magnitudes of visual extinction. The uncertainty in the colors for all sources is magnitude-dependent, but always ≤ 0.2 magnitudes, as labelled in both diagrams.

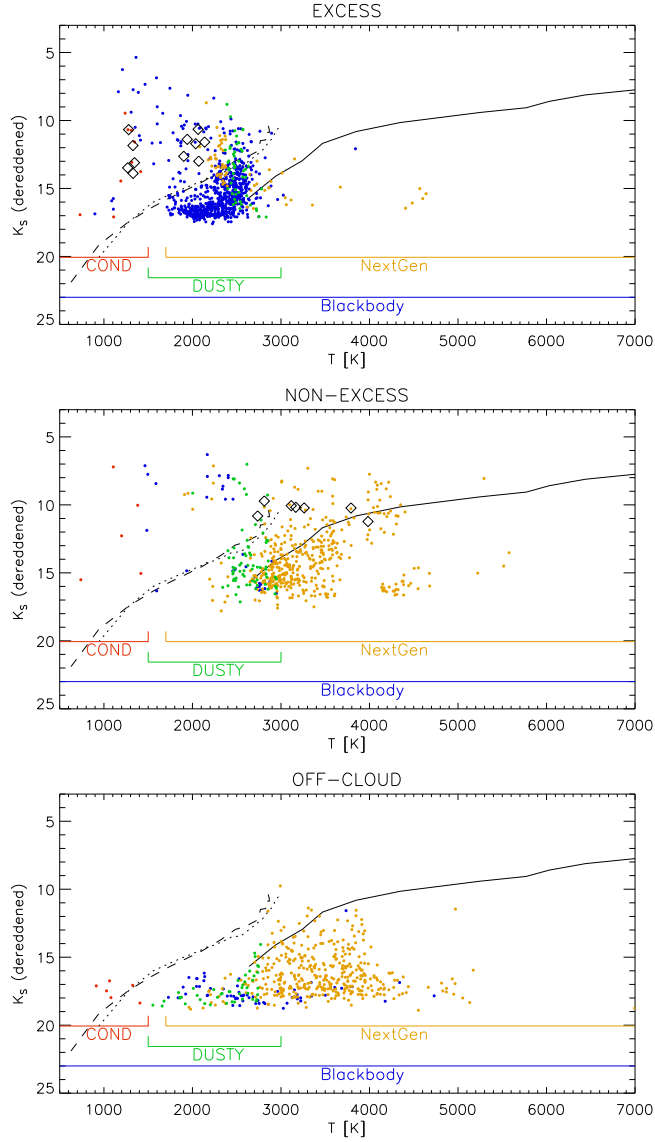


Fig. 4.— Dereddened K_s magnitude as a function of estimated temperature for sources for which successful SED fits were obtained to their JHK_s and *Spitzer* IRAC data. In the top panel, we plot the locations of the 827 “excess” sources, along with the locations of known, spectroscopically confirmed brown dwarfs with IR excesses, which are indicated by open diamond symbols. In the middle panel, we plot the locations of 527 “non-excess” sources, along with the locations of spectroscopically confirmed brown dwarfs lacking IR excesses, which are indicated by the open diamond symbols. In the bottom panel, we plot the locations of sources located in the cloud-exterior region from Marsh et al. (2010a). Model curves are plotted in each panel for the 1 Myr COND (dashed) and DUSTY (dotted) models, as well as for the main-sequence NEXTGEN models (solid), for an assumed distance of 124 pc.

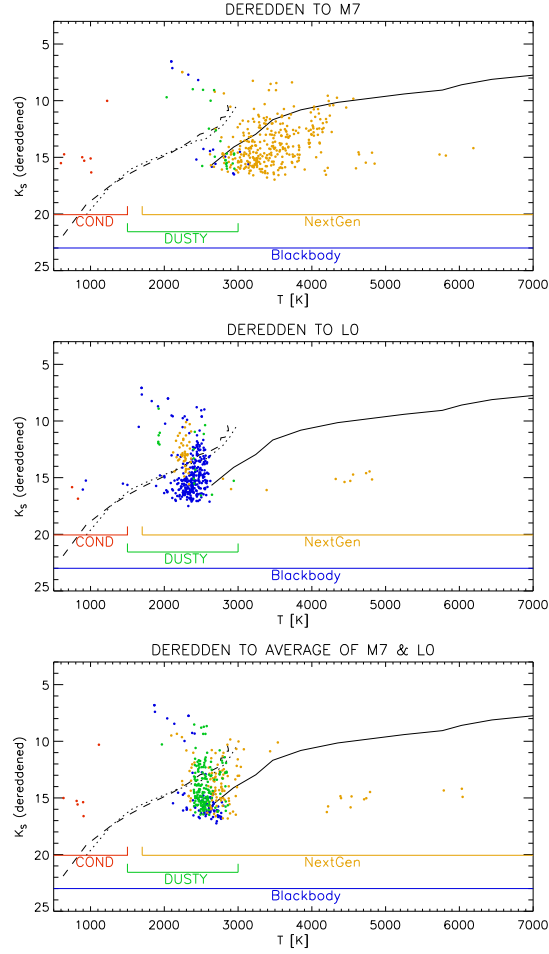


Fig. 5.— Same as Fig. 4, except for “non-excess” sources which de-redden to low-mass photospheric colors. The effect of assuming intrinsic $J - H$ vs. $H - K_s$ colors of M7 (top panel), L0 (middle panel), or to an average of M7-L0 spectral types (bottom panel) results in extinction values different enough to cause the demonstrated variation in the distribution of the best-fit SEDs in de-reddened K_s vs. T_{eff} space.

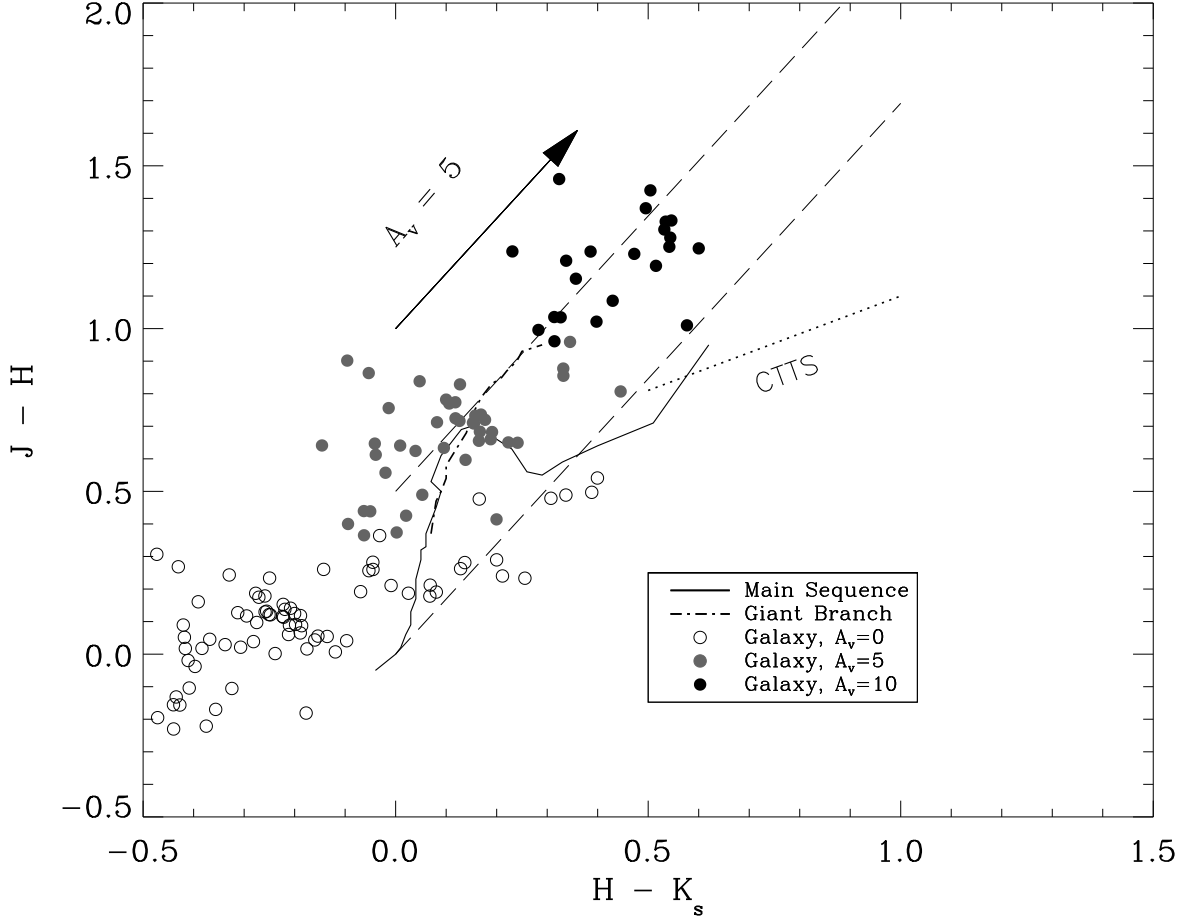


Fig. 6.— JHK_s color-color diagrams for all galaxies from the GOODS-South field to our completeness limits of $J = 20.0$, $H = 20.0$, $K_s = 18.50$ with no extinction (open circles), seen through $A_V = 5$ (grey circles), and seen through $A_V = 10$ (black circles). The loci of old main-sequence stars and substellar objects (solid curve), giants (dot-dashed line), and the Classical T-Tauri Star (CTTS) locus (dotted line) are all shown for clarity. The parallel dashed lines delineate the reddening band—objects in this region de-redden to main-sequence or giant colors. Comparison with Figure 3 shows that only a small fraction of background galaxies would fall into the “excess” region to the right of the right-most reddening line.

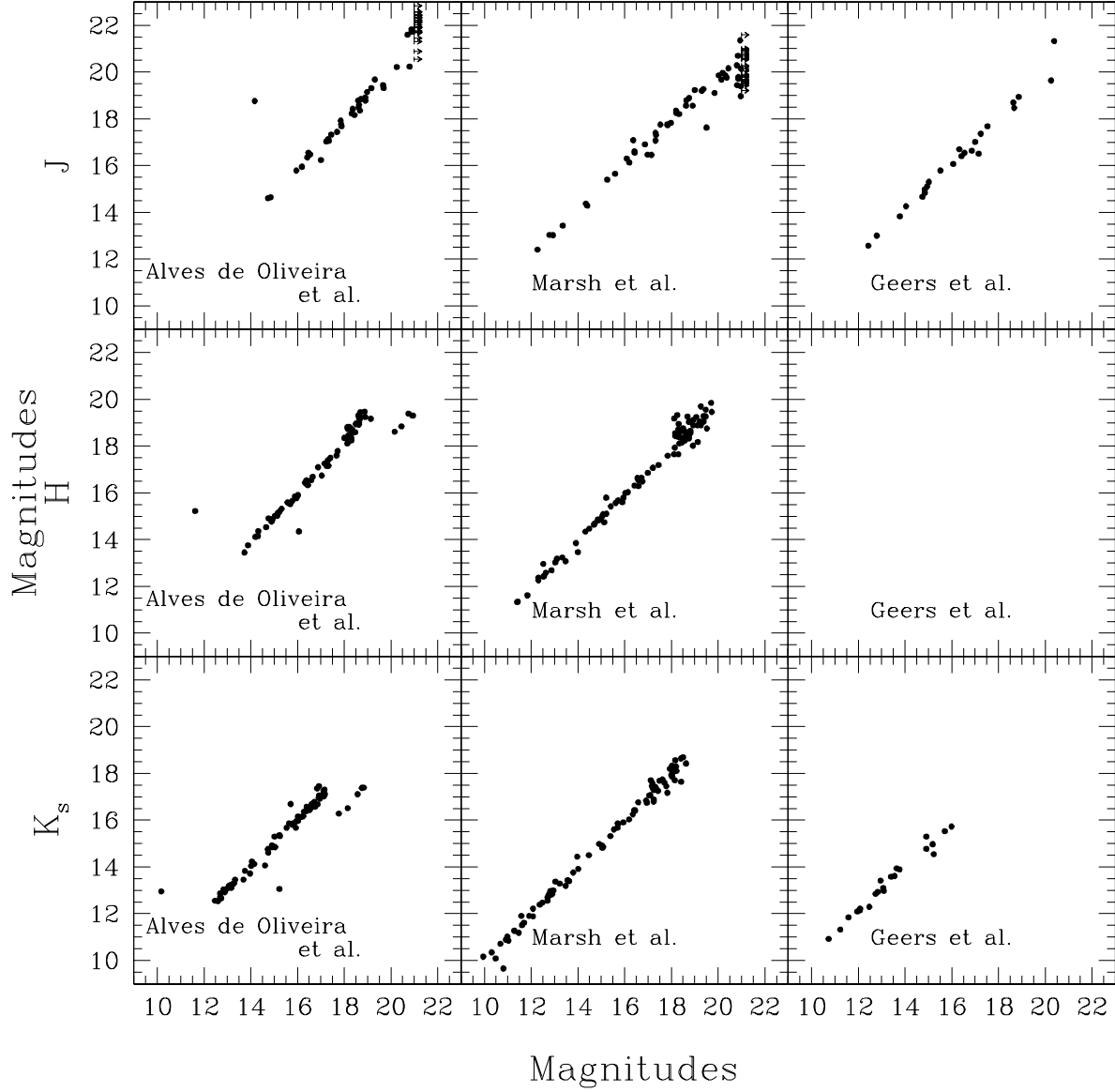


Fig. 7.— Comparison between photometry presented in this work (horizontal axes) with photometry published by other workers (vertical axes) for sources in common as presented in Table 4. Our non-detections at J -band are indicated by the rightward pointing arrows. No data are plotted at H -band for Geers et al. (2011), since they did not obtain H -band photometry.

Table 1. Nearby SFRs with Published IMFs Using NIR Imaging Data

SFR	Distance (pc)	Age (MYr)	Telescope IR Camera	FOV	J (mag)	H (mag)	K_s (mag)	Ref.
IC 348	300	2	KPNO 2.1m FLAMINGOS	$20.5' \times 20.5'$	18.82	18.04	17.72	(1)
			Calar-Alto 3.5m Omega Prime	$18.6' \times 18.4'$	19.5	... ^a	... ^a	(2)
ONC	430	0.8 ± 0.6	NTT 3.5m/SOFI + FLWO 1.2m/STELIRcam	$5' \times 5'$	18.15	18.7	17.5	(3)
Cha I	160-170	~ 2	2MASS + CTIO-4m/ISPI	$1.5^\circ \times 0.35^\circ$ $13.2' \times 16.8'$	15.75 18.5	15.25 18.25	14.3 ^b ... ^c	(4)
Taurus	140	$1-1.5^d$	2MASS	2.84 deg^2	15.75	15.25	14.3 ^a	(5)
		3^e	2MASS	1.32 deg^2				
σ Ori	360^{+70}_{-60}	3 ± 2	VLT 8.2-m ISAAC	790 arcmin^2	20.6	... ^a	... ^a	(6)
			UKIRT 3.8-m WFCAM	0.78 deg^2	19.0	18.4	18.0	(7)
ρ Oph	124	1	2MASS	$1^\circ \times 9.3'$	20.5	20.0	19.0	(8)
ρ Oph	124	1	AAO-3.8m IRIS2	920 arcmin^2	20.0	20.0	18.5	(9)

^aNo data acquired at this wavelength

^b2MASS K_s completeness from
http://www.ipac.caltech.edu/2mass/releases/allsky/doc/sec2_2b.html

^cData acquired, but K_s completeness limit not published

^dFor field centered at J2000 $\alpha=4^h 39^m 00^s$, $\delta=25^\circ 46' 00''$

^eFor field centered at J2000 $\alpha=4^h 55^m 00^s$, $\delta=30^\circ 24' 30''$

References. — (1) Muench et al. (2003); (2) Preibisch et al. (2003); (3) Muench et al. (2002);
(4) Luhman (2007); (5) Luhman (2004); (6) Caballero et al. (2007); (7) Lodieu et al. (2009);
(8) Marsh et al. (2010a); (9) This work

Table 2. Substellar Objects in Nearby SFRs

SFR	B.D./Star Ratio	Ref.	No. of Candidate PMO's ^a	Ref.
IC 348	15%–25%	(1,2)	1	(3)
ONC	30%	(4,5)	10	(6)
	54%	(7)	142-421	(7)
NGC1333	67%	(8)	0	(8)
Cha I	17%	(9)	10	(9)
Taurus	17%	(10)	0	(10)
σ Ori	23% ^b	(11)	17	(12)
Lupus	... ^c	(13)	0	(13)
ρ Oph	35% ^d	(14,15)	23	(16,17)

^aOnly isolated objects are listed here, thus leaving out TMR-1c in Taurus (Riaz & Martín 2011), the candidate PMO companion to 2M J044144 (Todorov et al. 2010), and the candidate PMO companion to Par-Lup3-4 (Comerón 2011).

^bfor d=352pc; 14% for d=440 pc

^cAlthough no substellar objects were found in the survey of (13), no definitive value for this ratio can be derived, due to small number statistics.

^dApproximation using 110 candidate substellar members (14) and 316 members (15).

References. — (1) Muench et al. (2003); (2) Luhman et al. (2003); (3) Burgess et al. (2009); (4) Slesnick et al. (2004); (5) Andersen et al. (2008); (6) Weights et al. (2009); (7) Robberto et al. (2010); (8) Scholz et al. (2009); (9) Mužić et al. (2011); (10) Luhman (2004) (11) Lodieu et al. (2009); (12) Fig. 2 of Bihain et al. (2009); (13) Comerón (2011); (14) Alves de Oliveira et al. (2010); (15) Wilking et al. (2008); (16) Marsh et al. (2010b); (17) Haisch, Barsony, & Tinney (2010)

Table 3. Rho Ophiuchi Low Mass Candidate Members^a

ID	RA ^b	Dec ^b	J	σJ	H	σH	K	σK	$I1$	$\sigma I1$	$I2$	$\sigma I2$	$I3$	$\sigma I3$	$I4$	$\sigma I4$	A_v ^c	Te_{ff} ^d	$Model$ ^e	IREX ^f
1	16:25:46.71	-24:18:13.6	17.92	0.07	16.48	0.04	15.31	0.04	0.351	0.034	0.254	0.023	0.418	0.327	-1.150	1.540	3.3	2099	B	E
2	16:25:46.74	-24:19:15.9	19.98	0.19	18.27	0.08	16.84	0.07	0.059	0.018	0.042	0.013	0.102	0.157	0.163	0.288	5.6	1959	B	E
3	16:25:46.80	-24:19:56.4	19.29	0.13	17.80	0.06	16.83	0.07	0.110	0.022	0.061	0.027	0.328	0.247	0.850	0.462	5.6	2234	B	E
4	16:25:46.84	-24:17:58.5	18.15	0.08	16.25	0.03	14.96	0.03	0.569	0.040	0.414	0.030	0.121	0.345	0.658	1.070	8.7	2401	B	E
5	16:25:46.92	-24:20:32.8	19.46	0.16	18.01	0.07	17.00	0.07	0.078	0.024	0.049	0.014	0.078	0.164	0.172	0.324	4.8	2190	B	E

^aTable 3 is published in its entirety in the electronic edition of the *Astrophysical Journal*. A portion is shown here for guidance regarding its form and content.

^bCoordinates listed are J2000. Units of right ascension are hours, minutes, and seconds, and units of declination are degrees, arcminutes, and arcseconds.

^cExtinction estimates were calculated by dereddening each source in the JHK color-color diagram as discussed in the text.

^dEffective temperatures obtained from model fits as discussed in the text.

^eModel used for best fit. B = Blackbody, D = DUSTY, C=COND, N=NextGen. See text for details.

^fInfrared Excess (E) or Non-Excess (NE) source.

Table 4. Photometric Comparison with Recent Sensitive NIR Surveys of ρ Oph

RA(2000)			Dec(2000)			This work			Alves de Oliveira et al.			Source No.	Marsh et al.			Source No.	Geers et al.	
<i>h</i>	<i>m</i>	<i>s</i>	$^{\circ}$	$'$	$''$	<i>J</i>	<i>H</i>	<i>K_s</i>	<i>J</i>	<i>H</i>	<i>K_s</i>		<i>J</i>	<i>H</i>	<i>K_s</i>		<i>J</i>	<i>K_s</i>
16	25	57.71	−24	23	17.56	17.89	14.92	13.04	8	17.68	14.84	13.11						
16	26	03.33	−24	30	25.02	17.87	16.45	15.25	9	17.76	16.33	15.32						
16	26	04.56	−24	17	51.32	15.51	13.45	12.06								12	15.79	12.19
16	26	07.24	−24	21	16.49	20.90	18.47	16.61	10	21.74	18.60	16.69						
16	26	07.92	−24	17	22.89	≥21.00	18.90	17.16	11	22.26	19.25	17.31						
16	26	11.69	−24	24	30.98	≥21.00	18.17	16.13	13	21.20	18.45	16.13						
16	26	13.16	−24	19	09.71	≥21.00	18.26	16.38	14	22.17	18.77	16.40						
16	26	16.27	−24	39	30.50	15.95	14.31	13.17	15	15.79	14.15	13.11						
16	26	18.62	−24	29	52.96	17.24	15.13	13.55								1	17.36	13.61
16	26	18.89	−24	26	10.95	14.85	13.25	12.06								13	14.84	12.14
16	26	19.06	−24	41	31.15	17.69	15.97	14.75	17	17.44	15.80	14.61						
16	26	19.26	−24	27	43.99	18.90	17.33	16.03	18	18.92	17.16	16.04						
16	26	21.46	−24	26	00.76	12.43	11.53	10.73								14	12.57	10.92
16	26	22.25	−24	37	08.27	18.98	16.88	15.64	19	19.15	17.10	15.86						
16	26	22.20	−24	24	06.58	16.32	14.83	13.64								2	16.70	13.94
16	26	23.84	−24	18	28.30	16.06	14.64	13.40								16	16.07	13.58
16	26	24.24	−24	15	52.53	17.53 ¹	15.48 ¹	14.02 ¹										
16	26	24.32	−24	15	48.07	18.60	15.90	13.75	21	18.78 ¹	15.85 ¹	13.83 ¹						
16	26	25.04	−24	41	33.51	17.23	15.69	14.61	22	17.03	15.52	14.06						
16	26	25.64	−24	37	27.81	18.33	16.59	15.39					1045	18.201	16.544	15.319		
16	26	25.98	−24	33	13.87	≥21.00	20.75	18.57	23	22.20	19.39	17.11						
16	26	26.44	−24	33	04.86	≥21.00	18.69	16.92	24	22.13	19.45	17.45						
16	26	27.76	−24	26	41.60	14.04	12.91	11.96								17	14.26	12.09
16	26	33.83	−24	18	52.96	≥21.00	20.91	18.84	25	22.42	19.31	17.39						
16	26	34.00	−24	35	55.88	≥21.00	19.44	17.47	26	22.45	19.31	17.38						
16	26	35.37	−24	30	11.15	≥21.00	18.01	15.93	27	22.32	18.35	15.94						
16	26	35.31	−24	42	40.93	19.31	17.72	16.28	28	19.68	17.79	16.36						
16	26	36.00	−24	20	58.65	18.72	15.77	13.69	29	18.84	15.65	13.46						
16	26	36.82	−24	18	59.99	17.00	16.06	15.23	30	16.24	14.35	13.06				3	17.01	14.55
16	26	37.84	−24	39	03.20	14.85	13.73	12.74	31	14.65	13.45	12.66				18	14.98	12.85
16	26	38.78	−24	23	22.20	14.94	12.81	11.42								2-3 ⁵	15.10	saturated
16	26	39.61	−24	18	02.90	≥21.00	18.67	17.18	32	22.55	19.15	17.11						
16	26	39.68	−24	22	07.51	18.44	17.04	15.93	33	18.16	16.74	15.68						

Table 4—Continued

RA(2000)			Dec(2000)			This work			Alves de Oliveira et al.				Marsh et al.			Geers et al.			
<i>h</i>	<i>m</i>	<i>s</i>	°	'	''	<i>J</i>	<i>H</i>	<i>K_s</i>	Source No.	<i>J</i>	<i>H</i>	<i>K_s</i>	Source No.	<i>J</i>	<i>H</i>	<i>K_s</i>	Source No.	<i>J</i>	<i>K_s</i>
16	26	39.92	−24	22	32.43	16.19	14.66	13.43	34	15.95	14.53								
16	26	40.03	−24	28	07.37	≥21.00	18.32	16.58	35	21.45	18.56	16.52							
16	26	40.58	−24	24	27.26	20.71	18.25	15.71	36	21.60	18.37	16.69							
16	26	40.85	−24	30	50.62	17.44	14.89	13.12	37	17.32	14.77	13.18							
16	26	41.80	−24	36	11.50	≥21.00	20.16	17.77	38	22.12	18.62	16.28							
16	26	41.83	−24	23	43.62	≥21.00	18.62	17.04	39	22.59	19.32	17.07							
16	26	42.73	−24	24	27.15	19.66	15.57	13.15	40	19.44	15.59	13.22							
16	26	43.78	−24	24	50.95	≥21.00	17.41	14.73	41	21.67	17.50	14.76							
16	26	48.45	−24	28	36.12	19.16	15.23	12.70	43	19.31	15.19	12.66							
16	26	48.75	−24	26	25.80	19.69	15.32	12.89	44	19.32	15.32	12.92							
16	26	50.91	−24	26	07.67	≥21.00	19.14	17.12	45	21.73	19.17	17.27							
16	26	51.22	−24	32	41.43	15.02	14.46	13.76									19	15.30	13.89
16	26	51.91	−24	30	38.62	≥21.00	16.32	13.33	46	21.30	16.43	13.45							
16	26	52.70	−24	24	52.85	≥21.00	18.30	15.78	48	21.76	18.24	15.80							
16	26	53.43	−24	32	35.67	20.88	16.65	13.29	49	21.83	16.69	13.30							
16	26	54.33	−24	24	38.59	≥21.00	17.16	14.02	50	21.71	17.25	14.04							
16	26	54.74	−24	27	02.40	17.85	14.76	12.69	51	17.92	14.91	12.87							
16	26	55.34	−24	21	17.10	≥21.00	18.37	17.23					4220	19.771	18.361	17.317			
16	26	55.47	−24	28	22.42	19.85	17.21	15.54					1518	19.105	17.075	15.601			
16	26	56.24	−24	16	18.05	14.34	12.53	11.69					108	14.373	12.424	11.615			
16	26	56.25	−24	21	30.90	≥21.00	18.75	17.34					4795	20.573	19.041	17.381			
16	26	56.32	−24	42	38.10	17.53	16.55	15.70					1254	17.753	16.633	15.865	2-1 ⁵	17.68	15.53
16	26	56.36	−24	41	19.85	18.63	16.42	14.91	53	18.60	16.34	14.92	829	18.567	16.309	14.981	4	18.70	14.77
16	26	56.87	−24	28	36.33	18.20	14.72	12.75					233	18.256	14.690	12.800			
16	26	57.34	−24	35	38.11	19.30	15.22	12.79					236	19.198	15.111	12.782			
16	26	57.37	−24	42	18.70	18.86	17.15	15.99									2-2 ⁵	18.94	15.73
16	26	58.43	−24	20	03.73	≥21.00	18.13	16.86	54	20.55	18.12	16.68							
16	26	58.35	−24	21	30.28	16.09	13.10	11.61					115	16.299	13.178	11.515			
16	26	58.67	−24	24	55.47	20.25	17.25	14.91	55	20.22	17.15	14.84					5	19.64	15.30
16	26	59.06	−24	35	56.54	17.15	14.00	12.08					141	16.459	13.464	11.882	6	16.51	12.21
16	26	59.94	−24	24	21.62	≥21.00	19.38	18.39					7614	20.740	19.286				
16	27	01.91	−24	22	06.47	20.03	15.62	13.48					291	19.853	15.573	13.196			
16	27	02.99	−24	26	14.68	≥21.00	15.72	12.70					207	...	15.673	12.559			

Table 4—Continued

RA(2000)			Dec(2000)			This work			Alves de Oliveira et al.				Marsh et al.			Geers et al.			
<i>h</i>	<i>m</i>	<i>s</i>	°	'	"	<i>J</i>	<i>H</i>	<i>K_s</i>	Source No.	<i>J</i>	<i>H</i>	<i>K_s</i>	Source No.	<i>J</i>	<i>H</i>	<i>K_s</i>	Source No.	<i>J</i>	<i>K_s</i>
16	27	03.57	−24	20	05.11	17.32	15.13	13.97	56	17.13	15.01	13.72	311	17.067	14.738	14.437			
16	27	04.09	−24	28	30.23	16.43	13.03	10.92					89	16.553	13.023	10.889			
16	27	04.54	−24	19	44.24	≥21.00	18.56	17.71					5598	20.239	18.642	17.607			
16	27	04.56	−24	27	15.21	16.98	13.47	11.47					103	16.464	13.076	11.185			
16	27	05.64	−24	40	12.85	20.94	16.72	14.01					439	21.353	16.645	13.911			
16	27	05.93	−24	18	40.18	17.34	15.94	15.05	58	17.05	15.77	14.85	654	17.307	15.784	14.816			
16	27	05.97	−24	28	36.73	16.86	14.58	13.09									20	16.64	12.97
16	27	05.98	−24	16	14.15	18.76	17.21	16.19					1344	18.889	17.069	16.032			
16	27	06.52	−24	18	32.18	20.19	18.35	17.63					6412	19.965	18.600				
16	27	06.62	−24	41	49.86	12.27	11.43	10.68					60	12.400	11.345	10.709			
16	27	07.00	−24	31	05.84	≥21.00	18.50	15.94					1558	21.587	18.758	15.909			
16	27	07.68	−24	34	03.04	≥21.00	18.63	16.75	59	22.33	19.00	16.58							
16	27	08.03	−24	20	06.87	17.83	14.99	13.63					312	17.768	14.851	13.397			
16	27	08.05	−24	31	42.32	≥21.00	19.18	18.12					7145	19.906	18.942	18.168			
16	27	08.14	−24	41	18.94	20.49	18.40	17.13					3253	19.696	18.467	16.800			
16	27	08.22	−24	42	29.97	15.25	12.31	10.81					74	15.393	12.261	9.656 ²			
16	27	08.44	−24	16	19.61	20.44	18.30	17.17					4933	20.158	18.726	17.468			
16	27	09.01	−24	30	25.31	≥21.00	18.61	16.02	60	22.14	19.30	16.15							
16	27	09.33	−24	24	04.58	20.97	18.47	17.19					4788	19.401	18.166	17.591			
16	27	09.36	−24	32	15.24	≥21.00	18.92	16.95					2438	19.701	18.018	16.741			
16	27	09.59	−24	24	17.93	≥21.00	18.59	18.17					5710	19.606	18.248	18.566			
16	27	09.80	−24	34	41.27	≥21.00	20.45	18.15	61	22.44	18.84	16.51							
16	27	10.05	−24	29	13.55	16.47	15.16	14.05	62	16.55	15.14	14.23							
16	27	10.20	−24	35	45.89	≥21.00	18.63	17.13	63	22.01	18.92	17.10							
16	27	10.33	−24	33	22.32	17.32	13.92	11.92					147	17.401	13.854	11.910			
16	27	11.28	−24	23	27.15	≥21.00	18.81	17.78					4863	19.503	18.568	17.460			
16	27	11.60	−24	23	21.80	20.31	18.16	17.19					4195	19.855	18.551	17.405			
16	27	11.64	−24	23	42.28	14.40	11.84	10.48					58	14.283	11.616	10.089			
16	27	11.95	−24	26	46.61	≥21.00	18.81	17.99					5820	20.136	18.657	17.925			
16	27	12.71	−24	32	0.00	≥21.00	19.26	18.20					14250	19.573	18.885	18.300			
16	27	13.01	−24	31	59.99	≥21.00	18.67	16.92	64	22.13	19.28	17.05	2978	19.474	18.380	16.840			
16	27	13.17	−24	23	47.60	≥21.00	17.67	15.53	65	20.88	17.60	15.67							
16	27	13.55	−24	34	14.43	≥21.00	19.57	18.21					9002	20.211	19.772	18.713			

Table 4—Continued

RA(2000)			Dec(2000)			This work			Alves de Oliveira et al.				Marsh et al.			Geers et al.			
<i>h</i>	<i>m</i>	<i>s</i>	°	'	''	<i>J</i>	<i>H</i>	<i>K_s</i>	Source No.	<i>J</i>	<i>H</i>	<i>K_s</i>	Source No.	<i>J</i>	<i>H</i>	<i>K_s</i>	Source No.	<i>J</i>	<i>K_s</i>
16	27	13.99	−24	32	06.19	≥21.00	18.94	17.62					5076	20.054	19.112	17.741			
16	27	14.08	−24	22	50.59	20.98	18.26	16.58					2956	20.144	18.405	16.759			
16	27	14.31	−24	31	31.85	18.36	16.38	15.02	66	18.42	16.53	15.30							
16	27	15.73	−24	38	43.68	14.17	11.62	10.17	67	18.76	15.22	12.95							
16	27	15.83	−24	25	13.93	20.80	16.02	13.22	68	20.23	15.90	13.26	313	20.289	15.988	13.283			
16	27	15.83	−24	34	06.74	≥21.00	19.07	17.49					5771	20.936	19.247	17.686			
16	27	15.90	−24	22	53.23	≥21.00	19.73	17.94					7906	21.006	19.460	18.198			
16	27	17.38	−24	32	06.97	≥21.00	17.84	15.73					1604	19.552	17.594	15.848			
16	27	17.40	−24	22	28.27	20.14	15.90	13.56					341	19.672	15.605	13.430			
16	27	18.17	−24	25	55.52	≥21.00	18.45	16.93					3872	20.056	18.355				
16	27	18.33	−24	24	25.75	16.87	13.33	11.28					107	16.907	13.229	11.271			
16	27	19.37	−24	20	49.25	20.89	18.30	16.24	71	21.73	18.35	16.17							
16	27	19.44	−24	26	00.82	≥21.00	18.34	16.72	70	21.71	18.71	16.79							
16	27	19.54	−24	26	21.28	≥21.00	18.63	18.04					5454	20.136	18.466	17.857			
16	27	19.79	−24	26	35.50	≥21.00	19.46	18.50					14819	20.280	19.272	18.697			
16	26	21.07	−24	28	28.55	≥21.00	18.79	17.30					4823	20.559	19.048	17.432			
16	27	21.21	−24	37	53.59	≥21.00	18.87	16.84	73	22.83	19.47	17.36							
16	27	21.55	−24	21	50.85	15.59	12.63	10.98					90	15.645	12.588	11.016			
16	27	21.66	−24	32	17.93	20.97	18.30	16.40					2403	18.968	17.650	16.421			
16	27	21.99	−24	29	38.29	19.77	15.41	12.90					238		15.424	12.838			
16	27	22.46	−24	38	37.44	≥21.00	18.63	16.96	74	22.20	19.19	16.92							
16	27	22.90	−24	18	26.38	≥21.00	19.26	18.03					5757	20.668	19.698	17.982			
16	27	22.97	−24	22	37.01	≥21.00	18.79	17.20					3809	20.587	18.893	17.066			
16	27	23.58	−24	30	46.55	≥21.00	19.13	17.26					4264	19.205	18.177	17.286			
16	27	23.59	−24	34	44.30	≥21.00	19.38	18.03					6745	19.838	19.049	18.329			
16	27	24.17	−24	25	10.86	≥21.00	18.16	15.81	75	22.32	18.73	15.85							
16	27	24.29	−24	20	44.72	≥21.00	18.69	17.05					5084	20.888	19.267				
16	27	24.37	−24	41	48.29	18.91	15.04	12.70	76	18.78	15.01	12.72	222	18.556	15.001	12.692			
16	27	24.60	−24	28	49.30	≥21.00	≥21.00	18.50					4077	19.920	18.673				
16	27	24.64	−24	34	22.04	≥21.00	18.15	16.45					2448	19.868	17.934	16.415			
16	27	24.67	−24	29	34.12	19.37	14.88	12.48					195	19.268	14.836	12.474			
16	27	25.42	−24	25	37.51	≥21.00	18.76	18.15					4450 ³	19.573	18.335	17.709			
16	27	25.62	−24	35	05.79	≥21.00	19.22	18.41					7704	19.653	19.054	18.642			

Table 4—Continued

RA(2000)			Dec(2000)			This work			Alves de Oliveira et al.				Marsh et al.				Geers et al.		
<i>h</i>	<i>m</i>	<i>s</i>	°	'	"	<i>J</i>	<i>H</i>	<i>K_s</i>	Source No.	<i>J</i>	<i>H</i>	<i>K_s</i>	Source No.	<i>J</i>	<i>H</i>	<i>K_s</i>	Source No.	<i>J</i>	<i>K_s</i>
16	27	25.64	−24	37	27.81	18.33	16.59	15.23	77	18.23	16.54	15.36							
16	27	25.75	−24	29	53.59	≥21.00	18.34	17.43					4114	19.204	18.119	17.253			
16	27	25.97	−24	28	56.75	≥21.00	19.52	17.83					2993	20.532	18.752	17.176			
16	27	26.18	−24	19	23.03	16.42	14.32	12.83	78	16.35	14.36	13.04	239	16.606	14.343	12.977	21	16.40	12.93
16	27	26.57	−24	25	54.39	12.79	12.31	11.58					93	13.033	12.373	11.909	22	13.00	11.84
16	27	26.62	−24	40	45.13	18.61	14.94	12.60	79	18.49	14.89	12.54							
16	27	27.09	−24	32	16.95	18.20	14.49	12.37					183	18.354	14.465	12.384			
16	27	27.68	−24	38	26.95	≥21.00	18.50	16.91	80	21.94	18.94	16.95							
16	27	28.18	−24	31	42.23	20.85	16.14	13.80					408	20.695	16.032	13.760			
16	27	28.71	−24	17	06.52	18.64	14.86	12.80					247	18.784	14.866	12.892			
16	27	29.30	−24	34	07.97	17.98	14.69	12.82					232	17.831	14.644	12.828			
16	27	29.46	−24	39	15.95	16.37	12.52	9.95 ²					62	17.088	12.966	10.162			
16	27	29.52	−24	19	44.80	≥21.00	19.70	18.63					9096	20.968	19.852	18.424			
16	27	29.68	−24	29	24.75	≥21.00	16.99	14.47					681	19.824	16.859	14.504			
16	27	30.56	−24	38	26.43	≥21.00	19.12	18.42					6740	19.418	18.886	17.647			
16	27	30.62	−24	32	34.41	12.94	12.55	12.08					101	13.022	12.453	12.213			
16	27	30.96	−24	20	01.74	≥21.00	18.12	17.06					3754	20.806	19.180	17.059			
16	27	31.07	−24	34	02.82	13.35	11.40	10.31					59	13.431	11.327	10.344			
16	27	31.77	−24	31	48.20	≥21.00	18.22	16.52	83	21.92	18.47	16.44							
16	27	32.19	−24	29	42.79	18.67	15.08	12.95	84	18.35	15.04	13.05	334		15.088	12.995	7	18.47	13.41
16	27	32.51	−24	16	04.20	≥21.00	18.14	16.39	85	22.42	18.81	16.57							
16	27	32.53	−24	39	46.07	20.87	18.11	16.35					2797	19.716	17.647	16.255			
16	27	32.70	−24	33	23.63	16.20	12.87	11.03					132	16.126	12.685	10.848			
16	27	32.70	−24	22	46.48	20.81	18.17	17.20					6419	19.441	18.436	17.425			
16	27	32.73	−24	32	41.83	19.00	15.21	13.04					491	19.231	15.795	13.377			
16	27	32.96	−24	28	11.15	20.87	17.45	15.02					1307	19.781	17.189	14.922			
16	27	33.55	−24	22	49.12	20.37	18.25	17.12					9558	19.768	19.332	17.708			
16	27	33.67	−24	30	50.99	≥21.00	18.31	17.24					5003	19.691	18.954	16.895			
16	27	33.81	−24	22	34.33	17.84	16.76	15.69					2870	17.725	16.491	15.672			
16	27	34.14	−24	33	08.37	≥21.00	18.50	17.14	87	22.22	18.96	17.03							
16	27	35.32	−24	39	57.61	19.50	16.59	15.08					2391	17.625	16.288	14.858			
16	27	37.20	−24	34	34.12	≥21.00	18.18	16.02	92	21.92	18.21	15.97							
16	27	37.24	−24	25	26.43	≥21.00	18.23	16.24	93	22.31	18.81	16.18							

Table 4—Continued

RA(2000)			Dec(2000)			This work			Alves de Oliveira et al.				Marsh et al.			Geers et al.				
<i>h</i>	<i>m</i>	<i>s</i>	°	'	''	<i>J</i>	<i>H</i>	<i>K_s</i>	Source No.	<i>J</i>	<i>H</i>	<i>K_s</i>	Source No.	<i>J</i>	<i>H</i>	<i>K_s</i>	Source No.	<i>J</i>	<i>K_s</i>	
16	27	37.40	−24	17	54.78	14.08	12.82	11.80										23	14.15	11.95
16	27	38.98	−24	40	20.53	16.54	14.20	12.47	94	16.48	14.12	12.56					8, 24 ⁴	16.54	12.29	
16	27	40.13	−24	26	36.60	≥21.00	17.30	14.15	95	21.90	17.39	14.13								
16	27	40.95	−24	28	59.55	14.74	13.88	13.07	96	14.60	13.76	13.19					25	14.66	13.10	
16	27	41.84	−24	42	34.99	20.38	17.47	15.18									9	21.32	14.97	
16	27	46.39	−24	31	41.02	13.78	12.28	11.23									26	13.83	11.32	
16	27	56.76	−24	28	16.74	≥21.00	19.47	18.22					6249	20.940	19.558	18.104				

¹Source 21 of Table 4 of Alves de Oliveira et al. is a 4.5'' binary in our images—their coordinates fall between those of the two components, whereas their photometry agrees with our photometry for the fainter component. We list the coordinates and photometry for the primary for completeness.

²Saturated in our data.

³This is the planetary mass object confirmed spectroscopically by Marsh et al. (2010b). See text for discussion.

⁴Sources 8 and 24 as listed in Geers et al.'s Table 1 have identical entries for their coordinates and photometry, with the exception of the K_s photometry which is listed at 13.36 for Source 8 and as 12.29 for Source 24. We have used the value listed for Source 24, as it agrees better with other determinations.

⁵Source No. from Table 2 of Geers et al. with spectroscopic follow-up.